Geophys. J. Int. (1992) **110,** 553–570

Modelling of laterally trapped surface waves with application to Rayleigh waves in the Hawaiian swell

Valérie Maupin*
Institut de Physique du Globe de Strasbourg, 5 rue Descartes, 67084 Strasbourg Cedex, France

Accepted 1992 March 23. Received 1992 March 23; in original form 1992 February 10

SUMMARY

A method for synthetizing surface wave seismograms in anelastic 2-D structures is presented. It is based on the local mode coupling method, extended here to allow for propagation in any direction, and especially in the symmetry direction of the structure. This implies including both homogeneous and inhomogeneous waves in the wavefield representation. The complex wavenumbers of inhomogeneous waves require that a dual space of modes and a new bi-orthonormality relation between modes are defined. Combinations of local modes which are not singular for modes having an horizontal turning point in the 2-D structure are used as a basis for wavefield decomposition. This allows calculation of the propagation and coupling characteristics of homogeneous and inhomogeneous waves with a single set of equations. The mode coupling matrices are then combined with source terms and boundary conditions to yield synthetic seismograms with a procedure similar to the one used in the reflectivity method in 1-D structures.

The method is applied to model Rayleigh wave fundamental modes propagating along the Hawaiian chain, in order to refine the interpretation of phase velocities measured for this area by Lévêque (1991). The *a priori* reheated and thinner lithosphere under the chain acts as lateral low-velocity waveguide where Rayleigh waves are trapped. We show that this waveguide has three lateral free modes in the period range 20 to 150 s. Synthetic seismograms for different source–receiver configurations are presented. The influence of the source-type, epicentral distance and channel width on the waveguide's amplification power is examined in the frequency domain. Apparent phase velocities between two stations situated in the middle of the channel are calculated, and the influence of the outer parts of the waveguide on these velocities is analysed. It is found that the velocities measured by Lévêque are probably influenced at 20 to 30 per cent by the normal lithosphere outside the reheated channel.

Key words: Hawaii, lateral heterogeneities, mode coupling methods, surface waves.

INTRODUCTION

Several types of elongated structures in the Earth act as corridors where surface waves are slower than in the surroundings. For long-period surface waves, the most common of these corridors are probably the young regions around the oceanic ridges, where phase velocities of Rayleigh waves are distinctly slower than in older regions (e.g. Forsyth 1977; Montagner & Jobert 1981). In this paper, we focus attention on surface wave propagation along another such kind of slow lateral channel: the lithosphere along the Hawaiian chain.

Geoid and heat flow data suggest that the asthenosphere presents a swell under the Hawaiian chain, the lithosphere getting reheated and thinner over a zone of about 1200 km width after having passed over the hot-spot (Detrick & Crough 1978). In order to see if seismological data may corroborate this reheating model, Woods *et al.* (1991) and Lévêque (1991) have measured and analysed dispersion of Rayleigh waves between two broad-band stations situated 2000 km from each other along the chain, on Hawaii and

* Present address: Institute of Geophysics, University of Oslo, PO Box 1022, 0315 Oslo, Norway.

Midway islands. By measuring the interstation phase velocity, they obtain information about the shear-velocity structure with depth in between the two stations, which can then be interpreted in terms of lithospheric thickness along the chain.

However, due to the wavelengths involved and the geometry of the wave paths along this *a priori* low-velocity corridor, it is not obvious which parts of the structure influence the data. In order to interpret the dispersion data in terms of a model for the Hawaiian swell, it is necessary to determine the respective influence of the central and outer parts of the corridor on the measured dispersions.

It is this influence that we quantify here, by presenting models of Rayleigh wave propagation in a model of the Hawaiian swell. Modelling methods exist for surface wave propagation in 3-D laterally heterogeneous structures (Snieder 1986; Bostock 1991). These very general methods are not well adapted here. The main reason is that we wish to take advantage of the 2-D nature of the structure in the modelling process. Therefore, starting from methods developed for surface wave propagation at small incidence across 2-D structures (Gregersen 1978; Kennett 1984; Maupin 1988), we extend them in order to allow for propagation at large incidence or along the structure. These extensions are presented in the first part of the paper. In the second part, seismograms are synthesized in a model of the Hawaiian swell constructed according to the reheating model. The amplification power of the channel and the characteristics of two-station dispersions in the channel are analysed.

LOCAL MODE COUPLING—EXTENSION OF THE METHOD

In order to model surface waves propagating mainly in the symmetry direction of a 2-D structure with continuous lateral variations, we generalize the local mode coupling method described in Maupin (1988), hereafter called M88. The formalism was originally restricted to waves propagating across the structure at non-grazing incidence (Fig. 1a). In order to allow for propagation in the symmetry direction, we need to include waves which propagate at grazing incidence in the channel as well as inhomogeneous waves in the wavefield representation (Fig. 1b). The formalism then needs to be extended to allow for the complex horizontal wavenumbers of these waves. Moreover, specific problems connected with surface waves having turning points inside the channel have to be solved. In the following, we give a description of the method with emphasis on the aspects of the coupling method which are new compared to M88. We also add some elements for transforming the mode coupling information into synthetic seismograms.

Wavefield decomposition on local modes with complex wavenumbers

The local mode coupling method is a spectral method using a Fourier decomposition of the wavefield in time and in the horizontal symmetry direction of the 2-D structure:

$$\mathbf{u}(x, p, z, \omega) = \int\int \mathbf{u}(x, y, z, t) \exp(ipy) \exp(-i\omega t)\, dp\, d\omega, \tag{1}$$

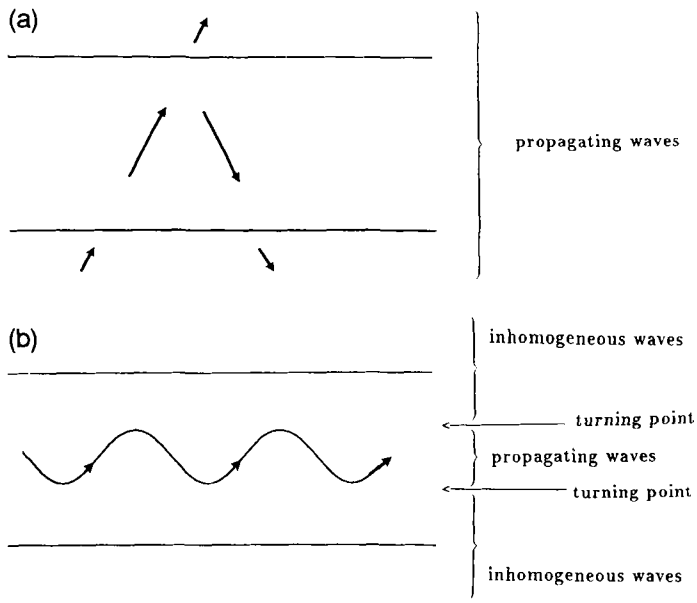

Figure 1. Plot (a)—wave propagation problem treated in Maupin (1988): transmission and reflection of surface waves across a channel. Plot (b)—wave propagation problem treated in this paper: waves laterally trapped inside a channel. The two parallel lines represent the sides of a slow-velocity channel, seen from above. The arrows show wave propagation directions. The type of wave needed to represent the wavefield in the different parts of the channel are indicated.

where x is the horizontal direction across the 2-D structure, y is the horizontal symmetry direction, and z is the vertical direction.

A first-order form in x of the equation of motion is used, acting on a six-component vector $\mathbf{u}$ combining displacement $\mathbf{w}$, and tension $\mathbf{t}_1$ on a vertical plane perpendicular to the x-axis:

$$\frac{\partial \mathbf{u}}{\partial x} = \mathbf{A}\mathbf{u} - \begin{pmatrix} 0 \\ \mathbf{f} \end{pmatrix} \quad \text{with } \mathbf{u} = \begin{pmatrix} \mathbf{w} \\ \mathbf{t}_1 \end{pmatrix}, \tag{2}$$

where $\mathbf{A}$ is an operator for the equation of motion, and $\mathbf{f}$ is the source term.

The basic assumption of the method is that the wavefield can be decomposed at each position x on the local modes, which are the modes of a laterally homogeneous structure having the same properties with depth as the local structure. We refer to M88 for the justification of this decomposition and to Maupin & Kennett (1987) for some numerical discussion pertaining to the truncation of the modal series in the decomposition. We analyse here only the characteristics of the local modes relevant for the extension of the method.

More precisely, the local modes $\mathbf{u}_i$ are defined as the independent solutions of equation (2) when the variation in x of $\mathbf{A}$ is considered as parametric. They satisfy the equation:

$$-ik_i\mathbf{u}_i = \mathbf{A}\mathbf{u}_i, \tag{3}$$

where k_i is the horizontal wavenumber in the x-direction (transverse to the channel).

In an isotropic or transversely isotropic model, k_i also satisfies:

$$k_i^2 + p^2 = K_i^2, \tag{4}$$

where K_i is the total horizontal local wavenumber of the mode, independent of p.

For real p and K_i, the wavenumber k_i may be either real or imaginary. The mode is then either propagating or inhomogeneous with exponentially varying amplitude in the x-direction. k_i may have positive or negative sign, corresponding to modes propagating or inhomogeneous, forward or backward in x. When $k_i = 0$, the mode is at a turning point in x. Modes with small k_i, at the transition between being propagating and inhomogeneous, are the most important ones when modelling the propagation close to the symmetry direction of the 2-D structure. Therefore, it is necessary to include modes which are inhomogeneous in x, and which had been explicitly excluded from the representation used in M88.

A new scalar product valid for complex wavenumbers

In order to perform the decomposition of the total wavefield on the local modes, a projection operator which gives an orthogonality relation between the modes is required. The projection operator used in Kennett (1984) and in M88 provides an orthogonality relation between modes having real p and k_i. The same scalar product may be used to derive an orthogonality relation in a somewhat more complicated form for inhomogeneous modes in elastic models (k_i imaginary). But it fails to give an orthogonality relation for complex values of p, as we will need when integrating in the complex p-plane, and for anelastic models.

Therefore, we derive a more general form for the orthogonality relation, valid for complex p and k_i values. In a similar way to the procedure used by Lognonné (1991) for calculating the coupling of the Earth's normal modes in anelastic models, we introduce a dual space of modes. The modes which satisfy the wave equation (2) with a reversed y-wavenumber $-p$ instead of p in $\mathbf{A}$ form this dual space. To a primal mode satisfying equation (3) is associated the dual mode $\mathbf{u}_i^{\#}$ which satisfies:

$$ik_i\mathbf{u}_i^{\#} = \mathbf{A}^{\#}\mathbf{u}_i^{\#}, \tag{5}$$

where $\mathbf{A}^{\#}$ is the dual operator.

If of propagating type, primal and dual modes are simply modes which propagate in opposite directions both in x and y. They are orthogonal with respect to the scalar product:

$$\langle \mathbf{u}^{\#}, \mathbf{u} \rangle = \int_0^{\infty} (\mathbf{w}^{\#}\mathbf{t}_1 - \mathbf{t}_1^{\#}\mathbf{w})\, dz. \tag{6}$$

Note that no complex conjugation is involved either in the definition of the scalar product or of the dual modes. The symmetry relations between primal and dual modes, the proof of their orthogonality and the symmetry properties of $\mathbf{A}$ with respect to the scalar product are detailed in Appendix A.

A modal decomposition non-singular at turning points

We now have a set of modes and dual modes satisfying a bi-orthogonality relation valid for complex p and k_i values. We wish to normalize them such that:

$$\langle \mathbf{u}_i^{\#}, \mathbf{u}_j \rangle = \delta_{ij}. \tag{7}$$

In isotropic and transversely isotropic models, we have for both Love and Rayleigh modes:

$$\langle \mathbf{u}_i^{\#}, \mathbf{u}_i \rangle = \frac{k_i}{K_i}\frac{2iU_iEc_i}{\omega}, \tag{8}$$

where U_i is the mode group velocity and Ec_i is its mean kinetic energy defined in Takeuchi & Saito (1972) as $\omega^2 \int_0^{\infty} \mathbf{w}^*\mathbf{w}\, dz$. In this expression, all the elements are independent of p, except k_i.

For propagating modes, $\langle \mathbf{u}_i^{\#}, \mathbf{u}_i \rangle$ is proportional to the flux of energy across a plane x = constant. When the mode reaches a turning point in x, the wavenumber k_i, the flux of energy, and $\langle \mathbf{u}_i^{\#}, \mathbf{u}_i \rangle$ go to zero. In this degenerate case, forward and backward modes are identical, and the scalar product (6) cannot be used simply to normalize the modes. Introducing anelasticity would solve the problem formally by adding an imaginary component to k_i. A more numerically stable solution to this problem is to decompose the wavefield on a new set of modes, which are not independent solutions of $\mathbf{A}$ anymore, but which have the great advantage of presenting no singularity at a turning point in x. These new modes, which we call basic modes since they form the basis for our wavefield decomposition, are:

$$\begin{aligned} \mathbf{u}_i^{+} &= \tfrac{1}{2}(\mathbf{u}_i + \bar{\mathbf{u}}_i), \\ \mathbf{u}_i^{-} &= \frac{1}{2}\frac{1}{-ik_i}(\mathbf{u}_i - \bar{\mathbf{u}}_i), \end{aligned} \tag{9}$$

where $\mathbf{u}_i$ is a forward mode, $\bar{\mathbf{u}}_i$ is the associated backward mode, and $\mathbf{k}_i$ has sign definition for the forward mode (see details in Appendix B).

They satisfy the equations:

$$\begin{aligned} -k_i^2\mathbf{u}_i^{-} &= \mathbf{A}\mathbf{u}_i^{+}, \\ \mathbf{u}_i^{+} &= \mathbf{A}\mathbf{u}_i^{-}. \end{aligned} \tag{10}$$

Their dual modes are:

$$\begin{aligned} \mathbf{u}_i^{+\#} &= \frac{1}{ik_i}(\mathbf{u}_i^{\#} - \bar{\mathbf{u}}_i^{\#}), \\ \mathbf{u}_i^{-\#} &= -(\mathbf{u}_i^{\#} + \bar{\mathbf{u}}_i^{\#}), \end{aligned} \tag{11}$$

and satisfy the equations:

$$\begin{aligned} -\mathbf{u}_i^{-\#} &= \mathbf{A}^{\#}\mathbf{u}_i^{+\#}, \\ k_i^2\mathbf{u}_i^{+\#} &= \mathbf{A}^{\#}\mathbf{u}_i^{-\#}. \end{aligned} \tag{12}$$

If the modal eigenfunctions are normalized such that:

$$\frac{2U_iEc_i}{\omega K_i} = 1, \tag{13}$$

one may verify that the basic modes are orthonormal:

$$\begin{aligned} \langle \mathbf{u}_i^{+\#}, \mathbf{u}_j^{-} \rangle &= \langle \mathbf{u}_i^{-\#}, \mathbf{u}_j^{+} \rangle = 0, \\ \langle \mathbf{u}_i^{+\#}, \mathbf{u}_j^{+} \rangle &= \langle \mathbf{u}_i^{-\#}, \mathbf{u}_j^{-} \rangle = \delta_{ij}. \end{aligned} \tag{14}$$

The six-component vectors $\mathbf{u}_i^{+}$ and $\mathbf{u}_i^{-}$, as a function of the Rayleigh and Love wave eigenfunctions, are given in Appendix B for transversely isotropic structures. With these

new modes, turning points are not singular cases anymore. Moreover, propagating, inhomogeneous modes, and modes with complex p and k_i values, satisfy the same equations of motion and bi-orthonormality relations. They do not require separate treatments when calculating their propagation or coupling characteristics.

Coupling across the structure

The procedure for calculating the coupling matrices in the structure is very similar to the procedure followed in M88. The expressions are somewhat more complicated because of the use of the new basic modes, which are not independent solutions of **A**. However, no new concept or element is introduced.

The total wavefield is decomposed on the basic modes:

$$\mathbf{u}(x, p, z, \omega) = \sum_{i=1}^{n} c_i^+(x, p, \omega)\mathbf{u}_i^+(x, p, z, \omega) + c_i^-(x, p, \omega)\mathbf{u}_i^-(x, p, z, \omega). \quad (15)$$

Constructing the total wavefield is now equivalent to solving for the different amplitude coefficients c_i^+ and c_i^- as a function of x.

Inserting the decomposition (15) into the equation of motion (2), and taking the scalar product with the dual modes, we obtain differential equations for c_i^+ and c_i^-:

$$\frac{\partial c_q^+}{\partial x} - c_q^- = -c_r^+\left\langle \mathbf{u}_q^{+\#}, \frac{\partial \mathbf{u}_r^+}{\partial x}\right\rangle - c_r^-\left\langle \mathbf{u}_q^{+\#}, \frac{\partial \mathbf{u}_r^-}{\partial x}\right\rangle,$$
$$\frac{\partial c_q^-}{\partial x} + k_q^2 c_q^+ = -c_r^+\left\langle \mathbf{u}_q^{-\#}, \frac{\partial \mathbf{u}_r^+}{\partial x}\right\rangle - c_r^-\left\langle \mathbf{u}_q^{-\#}, \frac{\partial \mathbf{u}_r^-}{\partial x}\right\rangle. \quad (16)$$

As in M88, the symmetry properties of the operator **A** with respect to the scalar product, may be used to transform the terms in $\left\langle \mathbf{u}_q^{\pm\#}, \frac{\partial \mathbf{u}_r^{\pm}}{\partial x}\right\rangle$ into terms in the symmetrized scalar product $\left\langle \mathbf{u}_q^{\pm\#}, \frac{\partial \mathbf{A}}{\partial x}, \mathbf{u}_r^{\pm}\right\rangle$, defined in Appendix A. The latter contain lateral derivatives of the elastic parameters, but not of the eigenfunctions. We obtain the following expressions when $r \neq q$:

$$\begin{pmatrix} \left\langle \mathbf{u}_q^{+\#}, \frac{\partial \mathbf{u}_r^-}{\partial x}\right\rangle \\ \left\langle \mathbf{u}_q^{-\#}, \frac{\partial \mathbf{u}_r^+}{\partial x}\right\rangle \end{pmatrix} = \frac{1}{k_r^2 - k_q^2}\begin{pmatrix} -1 & -1 \\ k_r^2 & k_q^2 \end{pmatrix}\begin{pmatrix} \left\langle \mathbf{u}_q^{-\#}, \frac{\partial \mathbf{A}}{\partial x}, \mathbf{u}_r^-\right\rangle \\ \left\langle \mathbf{u}_q^{+\#}, \frac{\partial \mathbf{A}}{\partial x}, \mathbf{u}_r^+\right\rangle \end{pmatrix}, \quad (17a)$$

$$\begin{pmatrix} \left\langle \mathbf{u}_q^{+\#}, \frac{\partial \mathbf{u}_r^+}{\partial x}\right\rangle \\ \left\langle \mathbf{u}_q^{-\#}, \frac{\partial \mathbf{u}_r^-}{\partial x}\right\rangle \end{pmatrix} = \frac{1}{k_r^2 - k_q^2}\begin{pmatrix} -1 & k_r^2 \\ -1 & k_q^2 \end{pmatrix}\begin{pmatrix} \left\langle \mathbf{u}_q^{-\#}, \frac{\partial \mathbf{A}}{\partial x}, \mathbf{u}_r^+\right\rangle \\ \left\langle \mathbf{u}_q^{+\#}, \frac{\partial \mathbf{A}}{\partial x}, \mathbf{u}_r^-\right\rangle \end{pmatrix}. \quad (17b)$$

Since several components of the eigenfunctions of the Love and Rayleigh basic modes are null, not all of the equations (17) are relevant for calculating the coupling for all mode pairs. Equation (17a) is non-zero only for pairs of Rayleigh modes or pairs of Love modes, whereas equation (17b) is non-zero only for a pair of a Love and a Rayleigh mode.

For $r = q$, some self-coupling terms are non-zero, and we define:

$$\gamma_r = \left\langle \mathbf{u}_r^{+\#}, \frac{\partial \mathbf{u}_r^+}{\partial x}\right\rangle = -\left\langle \mathbf{u}_r^{-\#}, \frac{\partial \mathbf{u}_r^-}{\partial x}\right\rangle = \frac{1}{2}\left\langle \mathbf{u}_r^{+\#}, \frac{\partial \mathbf{A}}{\partial x}, \mathbf{u}_r^-\right\rangle. \quad (18)$$

Using constraints on the local mode phase, the self-coupling terms could be put to zero in M88. It is not possible to do the same here because a pair of dual-primal modes can only be defined up to a factor $(f, 1/f)$, possibly complex and x-dependent. The self-coupling terms eliminate the dependence of the wavefield on this factor.

Inserting relations (17a) to (18) in the coupling equation (16), we obtain, in matrix form:

$$\frac{\partial \mathbf{c}}{\partial x} = \mathbf{D}\mathbf{c}, \quad (19)$$

where $\mathbf{c}$ is a $2 * n$ vector composed of the different (c_i^+, c_i^-) pairs, and $\mathbf{D}$ can be decomposed in $n^2(2 \times 2)$ submatrices d_{ij}.

Equation (19) is then used to construct propagators in x for the amplitude coefficient vector $\mathbf{c}$,

$$\mathbf{c}(x_1) = \mathbf{P}(x_2, x_1)\mathbf{c}(x_1). \quad (20)$$

We proceed in three steps for calculating this propagator. Intervals Δx are defined, for which the variations of $\mathbf{D}$ in x can be neglected. For each such interval, a first propagator is constructed which does not account for the mode coupling terms d_{ij}, $i \neq j$, but only for the diagonal submatrices. This first propagator describes phase and amplitude variations of the modes when they propagate independently through the structure. In the absence of very strong coupling effects, this propagator accounts for the dominant characteristics of the wavefield. It is composed only of diagonal terms $\mathbf{P}_i$, which are:

$$\mathbf{P}_i(x + \Delta x, x) = \begin{pmatrix} \frac{-\gamma_i}{\tilde{k}_i}\sin(\tilde{k}_i\Delta x) + \cos(\tilde{k}_i\Delta x) & \frac{1}{\tilde{k}_i}\sin(\tilde{k}_i\Delta x) \\ \frac{-k_i^2}{\tilde{k}_i}\sin(\tilde{k}_i\Delta x) & \frac{\gamma_i}{\tilde{k}_i}\sin(\tilde{k}_i\Delta x) + \cos(\tilde{k}_i\Delta x) \end{pmatrix} \quad (21)$$

where $\tilde{k}_i = \sqrt{k_i^2 - \gamma_i^2}$, and sin and cos are complex functions. Note that $\mathbf{P}_i$ is not singular when $\tilde{k}_i = 0$.

In a second step, the non-diagonal mode coupling elements are introduced at first order in Δx for constructing the total propagator:

$$\mathbf{P}(x + \Delta x, x) = \begin{pmatrix} P_1 & d_{12}P_2\Delta x & \cdots & d_{1n}P_n\Delta x \\ d_{21}P_1\Delta x & P_2 & \cdots & d_{2n}P_n\Delta x \\ \vdots & \vdots & \ddots & \vdots \\ d_{n1}P_1\Delta x & d_{n2}P_2\Delta x & \cdots & P_n \end{pmatrix}. \quad (22)$$

Finally, the different interval propagators are combined iteratively to obtain the global propagator between two positions in x in the structure.

Synthesis of the wavefield

Similar to the procedure used in the reflectivity method, the propagators are combined with source and boundary conditions in order to obtain the wavefield at the receiver position.

The source function, after Fourier transformation to the p and frequency domains, is expressed as discontinuities $\Delta\mathbf{c}^+(x)$ and $\Delta\mathbf{c}^-(x)$ in the modal amplitudes:

$$\Delta c_i^{\pm} = -\left\langle \mathbf{u}_i^{\pm\#}, \begin{pmatrix} 0 \\ \mathbf{f} \end{pmatrix} \right\rangle. \tag{23}$$

For a point-source with moment tensor $\boldsymbol{m}$, this can be replaced by:

$$\Delta c_i^{\pm} = -\boldsymbol{e}_i^{\pm\#} : \boldsymbol{m}, \tag{24}$$

where $\boldsymbol{e}_i^{\pm\#}$ is the strain tensor for the dual mode i at the source depth.

The boundary conditions can now be introduced. Only forward waves, as defined in Appendix B, are allowed outside the channel in the direction of increasing x, and only backward waves in the direction of decreasing x. The wavefield at a receiver located in x_r is then expressed as:

$$\mathbf{c}(x_r) = \int_{x_0}^{x_r} \mathbf{P}(x_r, \xi)\Delta\mathbf{c}(\xi)\, d\xi + \mathbf{P}(x_r, x_0)\mathbf{B}_0\mathbf{M}^{-1} \int_{x_0}^{x_1} \mathbf{P}(x_1, \xi)\Delta\mathbf{c}(\xi)\, d\xi, \tag{25}$$

where x_0 and x_1 are the channel boundaries, $\mathbf{M} = \mathbf{B}_1 - \mathbf{P}(x_1, x_0)\mathbf{B}_0$, $\mathbf{B}_0$ expresses the boundary conditions at x_0:

$$\mathbf{B}_0 = \begin{pmatrix} 1 & 0 & 0 & 0 & \dots & 0 & 0 \\ ik_1 & 0 & 0 & 0 & \dots & 0 & 0 \\ 0 & 0 & 1 & 0 & \dots & 0 & 0 \\ 0 & 0 & ik_2 & 0 & \dots & 0 & 0 \\ \vdots & \vdots & \vdots & \vdots & \ddots & \vdots & \vdots \\ 0 & 0 & 0 & 0 & \dots & 1 & 0 \\ 0 & 0 & 0 & 0 & \dots & ik_n & 0 \end{pmatrix},$$

and $\mathbf{B}_1$ expresses the boundary conditions at x_1:

$$\mathbf{B}_1 = \begin{pmatrix} 0 & 1 & 0 & 0 & \dots & 0 & 0 \\ 0 & -ik_1 & 0 & 0 & \dots & 0 & 0 \\ 0 & 0 & 0 & 1 & \dots & 0 & 0 \\ 0 & 0 & 0 & -ik_2 & \dots & 0 & 0 \\ \vdots & \vdots & \vdots & \vdots & \ddots & \vdots & \vdots \\ 0 & 0 & 0 & 0 & \dots & 0 & 1 \\ 0 & 0 & 0 & 0 & \dots & 0 & -ik_n \end{pmatrix}.$$

Note the presence of an inverse matrix $\mathbf{M}^{-1}$ in equation (25). In elastic models, the determinant of $\mathbf{M}$ is zero for a finite number of p values. At these poles of the coupling equation, non-trivial solutions exist which satisfy the boundary conditions on both sides of the channel without any source term. These free solutions are lateral modes of the structure for which dispersion curves and eigendisplacements as a function of x and z may be calculated. They play a dominant role in the wavefield at large distances from the source.

Inserting the coefficients $\mathbf{c}(x_r)$ in expression (15), we obtain the wavefield at the station in the wavenumber and frequency domains. In order to obtain the wavefield in the space domain, a Filon integral is performed in the complex p-plane along a contour similar to the one proposed by Frazer & Gettrust (1984) for wavenumber integrals in the reflectivity method. In order to avoid problems around the poles of the integrand, we work only with anelastic models, where the poles are moved off the real p-axis. Finally, an inverse Fourier transform yields synthetic seismograms in the time domain.

MODELLING OF RAYLEIGH WAVES IN THE HAWAIIAN SWELL

The method described above will now be used to calculate synthetic seismograms for different source–station configurations in the Hawaiian swell, and to analyse the apparent dispersion between stations situated in the channel. We choose the model so that it reflects as well as possible the expected structure of the swell between Hawaiian and Midway islands according to the reheating model.

Model of the swell

Geoid and heat-flux data suggest that the lithosphere under the Hawaiian swell is thinner than normal lithosphere of the same age. According to Detrick & Crough (1978), this thinning may be due to a reheating of the lithosphere by the hotspot, equivalent to a rejuvenation which puts the structure back to a 25 Myr old stage when it passes over the hotspot. Woods *et al.* (1991) have compiled information about the age of the structures between Hawaii and Midway islands in order to predict the lithosphere structure in this region according to the reheating model. Considering the

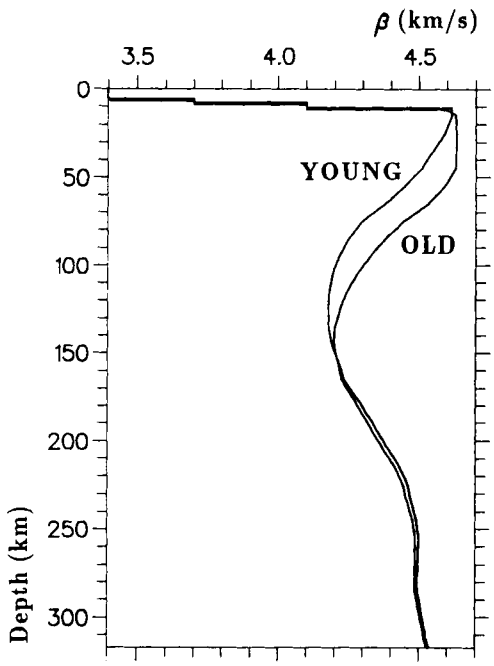

Figure 2. S-wave velocities as a function of depth in the models of Nishimura & Forsyth (1989) for a 20–52 Myr Pacific lithosphere (labelled young), and a 52–110 Myr Pacific lithosphere (labelled old), used as extreme models of our 2-D swell structure.

age of the hotspot features on Hawaii and Midway islands, of 3 and 28 Myr respectively, they find that the lithosphere along the swell is expected to be equivalent to a 28–52 Myr one. In the region between the two islands but outside the swell, the normal oceanic lithosphere is between 85 and 110 Myr old. They conclude that two Pacific Ocean models of Nishimura & Forsyth (1989) should be very well adapted to describe the lithosphere respectively in the middle and at the outskirts of the swell: the one for the lithosphere between 20 and 52 Myr old, and the one for the lithosphere with age between 52 and 110 Myr. These two models are transversely isotropic. Their *S*-wave velocities with depth are presented in Fig. 2. We also choose them to construct a model of the 2-D channel, continuous in x. The model for the oldest lithosphere is used to represent the structure with depth outside the swell and on its boundaries. The model for the youngest lithosphere is used to represent the structure with depth in the middle of the channel. For any other x-position inside the channel, the model with depth is defined by interpolating between these two extreme models with one period of a cosine function. The width of the channel is taken as 1200 km, in accordance with the observations of Detrick & Crough (1978). Calculations with a more narrow channel of 300 km are also performed in order to analyse the influence of the channel width on the results.

Modal representation of the wavefield

We are primarily interested in studying the dispersion of the Rayleigh wave fundamental mode in the swell. Therefore, this mode has to be included in the set of modes used to represent the wavefield. The higher Rayleigh modes and the Love modes which are coupled through the structure with the Rayleigh fundamental mode should also be included. In order to test this coupling, we have performed calculations adding to the Rayleigh wave fundamental mode either the Rayleigh wave first overtone, either the Love wave fundamental mode. The source was artifically constrained to generate only Rayleigh wave fundamental modes, so that all contributions to the wavefield from higher modes would come only from coupling through the structure. In all cases, the effect of the coupling was extremely small and could hardly be detected.

That no coupling with higher modes occurs when a Rayleigh wave fundamental mode propagates through the Hawaii swell can be explained by the combination of two factors. First, the model is a smooth long-wavelength structure. Therefore only modes having very similar wavenumbers may couple in this structure. Second, due to its very low phase velocity, the Rayleigh wave fundamental mode always has a wavenumber rather different from the wavenumbers of the other modes. It is therefore a very stable mode which couples with other modes only in the presence of rather sharp heterogeneities, absent in the Hawaiian swell.

For the synthetic seismograms and dispersion curves presented below, only the fundamental Rayleigh wave mode has been included in the representation of the wavefield, since it is the only one which appears to be necessary. Its dispersion and vertical eigenfunctions in the different reference structures are calculated with a program package from Saito (1988), in which the sphericity of the Earth is accounted for. The local mode coupling method is derived for flat structures only. Therefore, the sphericity of the Earth in the direction transverse to the channel is neglected in the calculations presented below. However, we will evaluate the order of magnitude of the errors introduced by this approximation.

The 2-D structure is defined as a cosinusoidal interpolation between two extreme models. For calculating the different elements for the synthetization of the wavefield, namely the propagators (equation 20) and the excitation terms (equation 24), we have to map the local wavenumbers and eigenfunctions in this structure as a function of x. In practice, we need to determine how often in x we should recalculate the local wavenumbers and eigenfunctions with Saito's programs in order to obtain a satisfactory approximation of the wavefield.

The wavenumbers appear as isolated elements in the propagators and play a prominent role in the characteristics of the wavefield. It is therefore necessary to have a precise representation of their variation with x. However, wavenumbers vary rather linearly with structural variations. In order to evaluate the degree of linearity in our 2-D structure, we compare the mean of their extreme values, computed in the extreme models of the structure, with their value in the mean model of the structure. We find differences of 0.03 to 0.06 per cent, which, compared to the difference between the extreme wavenumbers, is of the order of 1 to 2 per cent. Considering this very good linearity, the wavenumbers, as a function of x, can be evaluated by a direct cosinusoidal interpolation between their extreme values.

The terms which involve an integral with depth of the modal eigenfunctions have a first-order variation in $\sin(x)$, which arises from the lateral derivatives of the elastic coefficients and from interface slopes. The variations in x of the eigenfunctions, which would contribute as second-order terms only, are not very large for the Rayleigh wave fundamental mode (for example 10 per cent at a period of 28 s). They can be neglected and the eigenfunctions calculated only in the mean model between the two extreme models of the structure.

Therefore, we calculate the local modes in only three models: the two extreme models, to obtain the extreme wavenumbers in the structure, and the mean model in order to have the eigenfunctions to be used in the self-coupling or coupling terms.

The attenuation is laterally homogeneous in the model, and is taken identical to the attenuation in the internal model. The synthetic seismograms are computed between periods of 20 and 150 s, and convolved with the response of an High Gain Long Period instrument.

Lateral modes

Before presenting any synthetic seismogram, we analyse the characteristics of the lateral modes in our two channel models. Their dispersions are computed by searching for the poles of the coupling equation in structures made perfectly elastic. Inside the channel, the eigenfunctions are calculated by following the evolution of the wavefield through the structure when propagating the boundary conditions on one

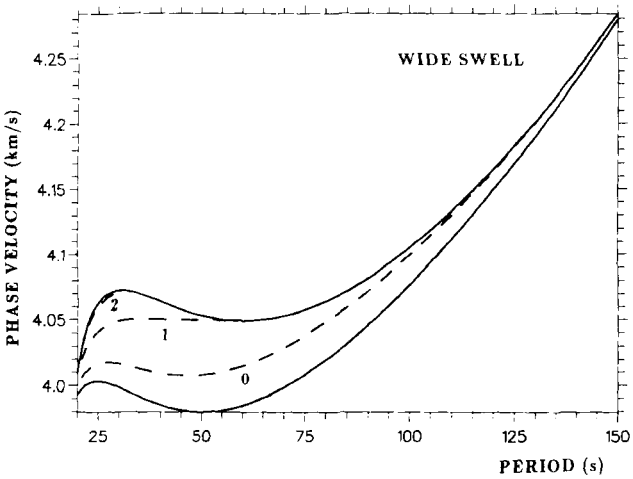

Figure 3. Phase velocities as a function of period for the three lateral modes of a 1200 km wide swell. The dotted lines show the phase velocities of the fundamental lateral mode (labelled 0), the first (1), and the second higher lateral mode (2). For reference, the phase velocities in the models of Nishimura & Forsyth (1989) for a 20–52 Myr Pacific lithosphere (lower solid curve), and a 52–110 Myr Pacific lithosphere (upper solid curve) are shown.

side of the channel to the other side. They can be extended outside the channel with the appropriate exponential functions.

For the 1200 km wide channel, three lateral modes exist for the Rayleigh wave fundamental mode between 20 and 150 s of period. Their dispersion curves are shown in Fig. 3. The two higher modes have cut-off periods at 56 and 33 s. Only the fundamental mode exists over the whole period range. Its three displacement components at 28 s of period are shown in Fig. 4(a). They show that this mode is dominantly symmetric, only its small x-component being antisymmetric. The displacement which is plotted corresponds to the displacement at the surface of the model. The displacement at depth may be obtained by modulating these surface displacements by the vertical Rayleigh wave displacement for the z-component, and by the longitudinal displacement for the x and y-components. The surface vertical displacement of the first and second higher modes, dominantly antisymmetric and symmetric modes respectively, are shown at 28 s of period in Fig. 4(b).

For the 300 km channel, only the fundamental mode exists at periods larger than 20 s (Fig. 5). The vertical components of the surface displacement at 28 and 60 s in the wide and in the narrow channel can be compared in Fig. 6. The absolute amplitudes of the eigenfunctions are arbitrary, and have been chosen here to facilitate comparison. It appears that the shape of the eigenfunctions is not very dependent on the swell width.

Seismograms for a source in the middle of the channel

We now present synthetic seismograms produced by a source situated in the middle of the channel. In order to avoid superposing a source radiation pattern on the amplitude variations related to the channel itself, we use an explosive source. The influence of the source mechanism on the results compared to the effect of the channel itself has been checked by performing the calculations with various source mechanisms. It is small, typically a few per cent in amplification variations at the largest epicentral distances, as long as we do not consider seismograms in a direction close to a node of the radiation pattern.

The stations are placed at 1000, 3000 and 5000 km from

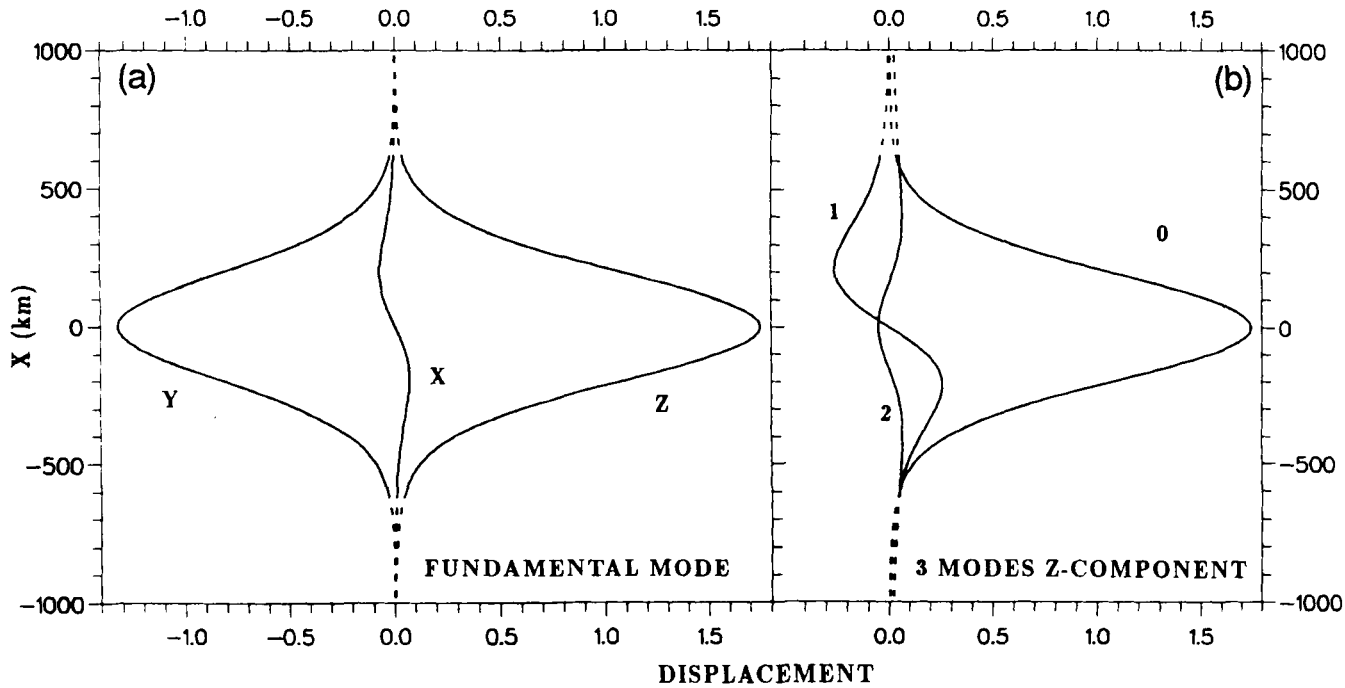

Figure 4. Surface displacement of the lateral modes as a function of position x in the 1200 km swell at a period of 28 s. On plot (a) are shown the three components of the fundamental lateral mode, and on plot (b) the vertical components of the three lateral modes. The displacements inside the swell are shown as solid lines, and outside the swell as dotted lines.

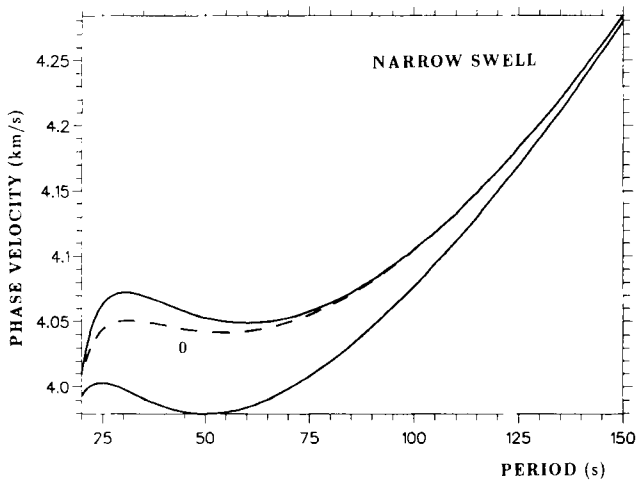

Figure 5. The same as Fig. 3 for the unique lateral mode of a 300 km wide swell.

the source along the channel axis, and at seven different offsets from this axis. The vertical components of the synthetic seismograms produced by a source at 15 km depth are shown in Fig. 7. The amplitudes are normalized for each set of seven plots at the same epicentral distance along the axis.

Despite the small contrast between the two extreme models of the structure, which reaches only 1.5 per cent at the maximum in phase velocity, and its large wavelength of 1200 km, the waveguide effect of the lateral channel is very clear at large epicentral distances. In the case presented here, the waveform itself is changing little, but the amplification of the signal in the middle of the channel is significant.

In order to get more insight into the amplification power of the channel, we compare the amplitude spectra of the synthetic seismograms calculated in the laterally heterogeneous structure with those of synthetic seismograms computed in an homogeneous model. The latter is chosen identical to the model in the middle of the channel. Fig. 8(a) presents the spectral amplitude ratios of the seven seismograms of Fig. 7 at about 3000 km epicentral distance, relative to a seismogram at the same epicentral distance in the homogeneous model. The amplification is largest within 100 km around the middle of the channel, with a peak of 1.25 at 35 s of period. There is a slight decrease of amplitude at the shortest periods when the station is situated at the outskirts of the swell.

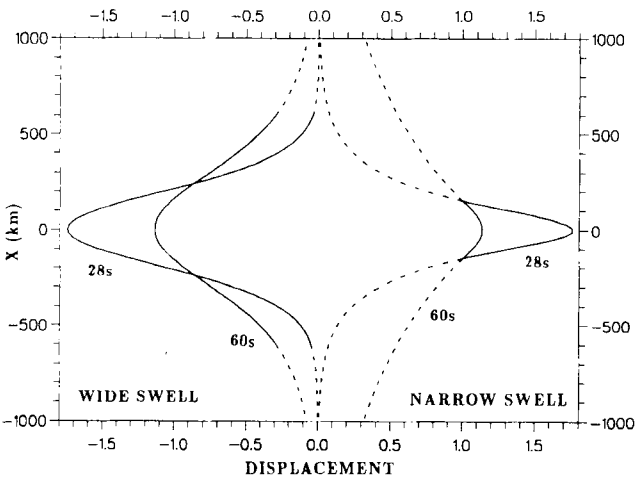

Figure 6. Surface displacement of the fundamental lateral mode as a function of position x at periods of 28 and 60 s in the 1200 km swell (left side curves) and in the 300 km wide swell (right side curves). The displacements inside the swells are shown as solid lines, and outside as dotted lines. The normalization of the different curves is chosen to facilitate their comparison.

Fig. 9 presents synthetic seismograms for the same source–station configurations as in Fig. 7, but for a more narrow swell of 300 km width. In this case, 15 out of the 21 stations are located outside the channel. The waveforms are more affected by the lateral heterogeneity. The amplitude variations between the different stations are larger and appear at smaller epicentral distance than in the wider swell. As can be seen from Figs 8(b) and 10, this trend is even more clear in the frequency domain. Besides, the amplification occurs in a more restricted frequency band and at shorter periods in the narrow swell.

Seismograms for a source offset by 600 km from the channel axis

The effect of the channel is of course also dependent on the source position. When the source is situated at 600 km from the channel axis, that is at the outer boundary of the wide swell and at 450 km from the narrow one, the amplitude of the Rayleigh wave vertical component is less dependent on the receiver offset, as can be seen in Figs 11 and 12. The main effect of the waveguide is to produce resonance at the shortest periods, which lengthens the wavetrains. In the wider channel, the spectral amplitude is slightly decreased at all stations (Fig. 13a). The variations of amplification with frequency are more complex and station dependent in the narrow channel (Fig. 13b).

When the source is far off the channel axis, the energy which reaches the stations departs from the source in different directions in the homogeneous and in the laterally heterogeneous structures. This direction difference is frequency dependent. Therefore, the radiation pattern at the source influences the amplification curves more than when the source lies in the middle of the channel. However, as long as the source–station direction is not close to a node of the source radiation pattern, this effect is small compared to the effect of the lateral heterogeneity itself.

Seismograms for a line-source

The Hawaiian swell is not the infinite 2-D structure that we are using in our models. It has a finite length of about 3000 km, starting at Hawaii, and turning north 1000 km north-west of Midway island. Therefore, the seismic sources that Woods *et al.* (1991) and Lévêque (1991) utilize to obtain dispersion data between Hawaii and Midway stations are not situated inside the swell. Rather, they produce a wavefront which enters the swell at one or its other end.

In order to approach this situation better, we can replace the point-source used in the previous examples by a line-source situated at right angles through the structure,

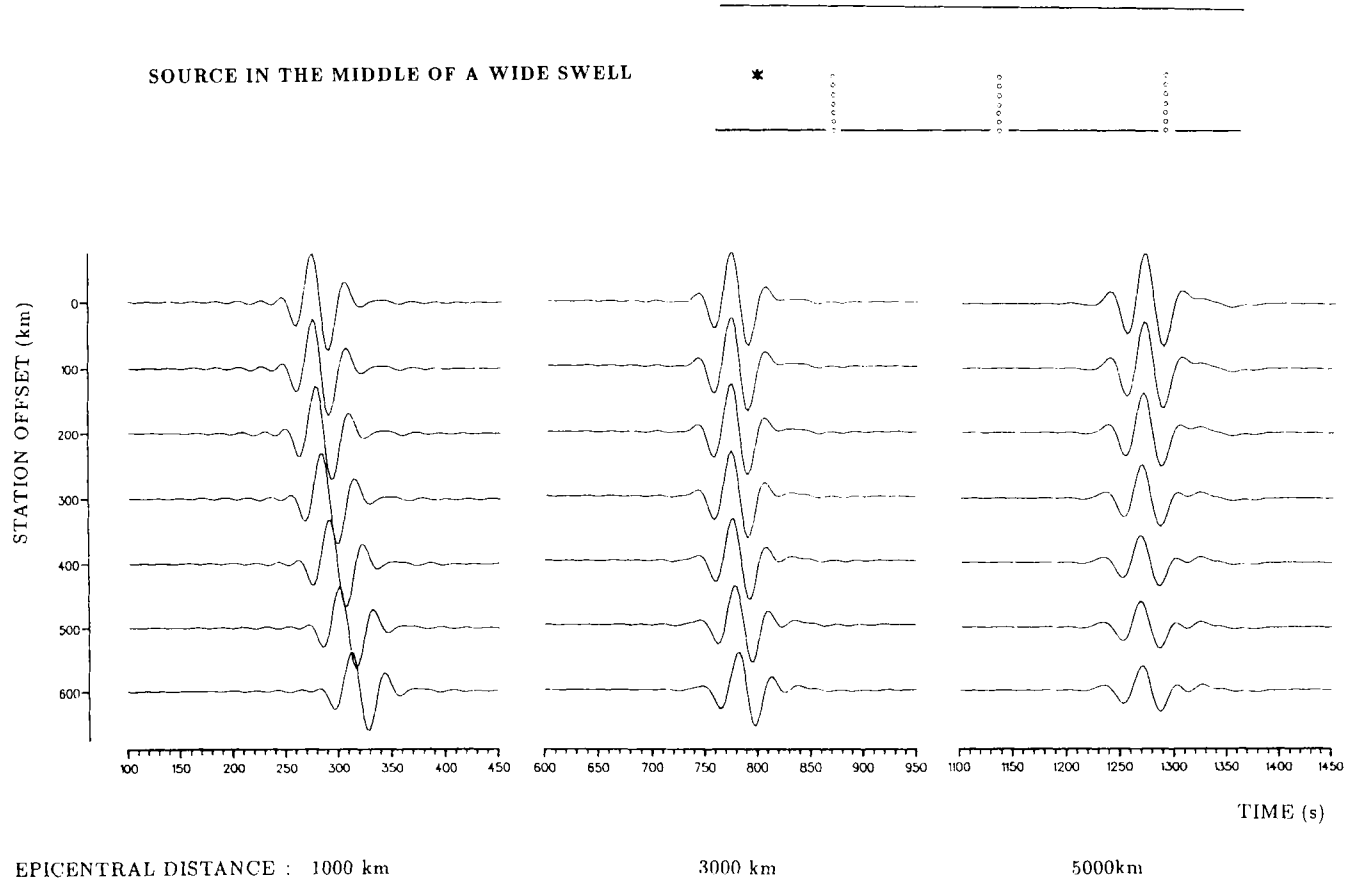

Figure 7. Vertical components of Rayleigh wave synthetic seismograms for propagation in a 1200 km wide swell. The source is an explosion at 15 km depth in the middle of the swell. The stations are situated every 100 km on lines perpendicular to the swell axis, at 1000, 3000 and 5000 km epicentral distance, as shown on the diagram in the top right corner of the figure. The seven seismograms at a given epicentral distance are normalized to the same vertical scale. Timing is relative to the source time.

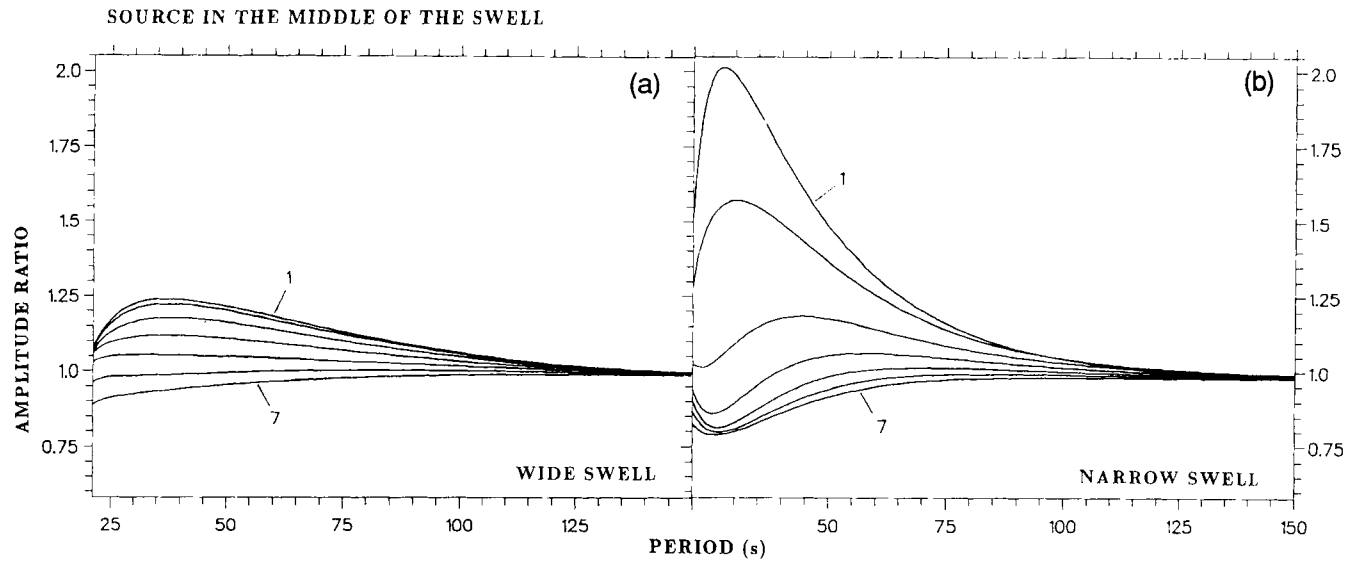

Figure 8. Spectral amplitude ratios for the vertical components of Rayleigh wave synthetic seismograms propagating in a 1200 km wide swell (plot a), and in a 300 km wide swell (plot b). The source is an explosion at 15 km depth in the middle of the swell. The stations are situated every 100 km on lines perpendicular to the swell axis at 3000 km epicentral distance. The amplitude ratio is varying continuously with station offset, from null offset (curve labelled 1), to 600 km offset (curve labelled 7).

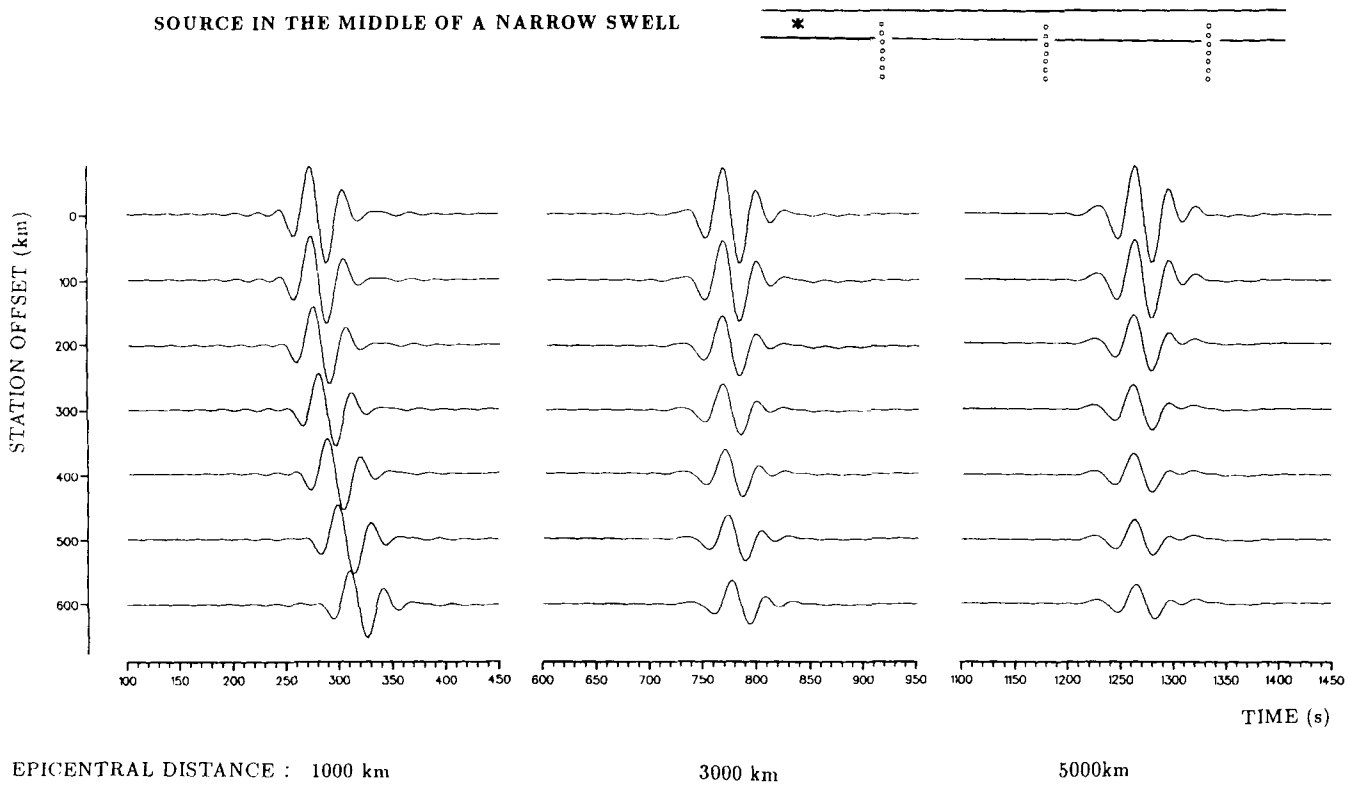

Figure 9. The same as Fig. 7 for a swell of 300 km width.

and extending to infinity on both sides in the homogeneous external structure. Synthetic seismograms for such line-sources are shown in Fig. 14 for the wide swell, and in Fig. 15 for the narrow one. At large epicentral distances, the waveforms are more affected by the lateral heterogeneity than they were when produced by a point-source. A particularly interesting example in Fig. 14 at 5000 km epicentral distance shows how an early arriving phase, visible at the station at 600 km from the channel axis, interferes destructively at 300 km with the later arriving phase, dominant in the middle of the swell.

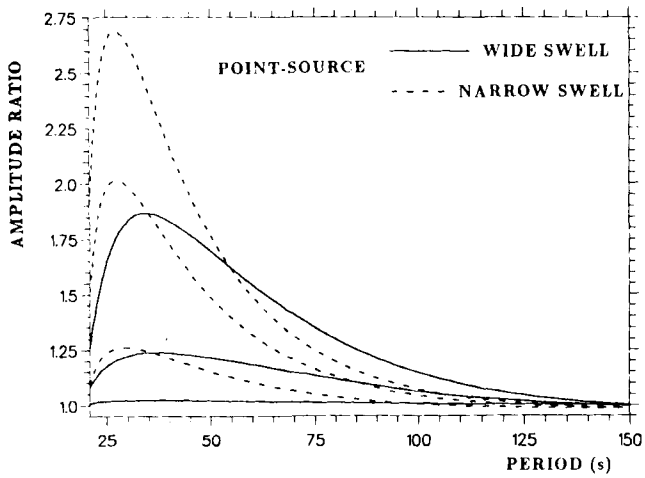

Figure 10. Spectral amplitude ratios of the vertical components of Rayleigh wave synthetic seismograms for propagation in a 1200 km wide swell (solid lines), and in a 300 km wide swell (dotted lines). The source is an explosion at 15 km depth in the middle of the swell. The stations are situated on the swell axis at 1000, 3000 and 5000 km epicentral distance. The amplification is increasing with epicentral distance.

Fig. 16 shows the spectral amplitude ratios for a line-source signal in the middle of the swell at an epicentral distance of 3000 km both for the wide and the narrow swell. The difference in amplification between the two swells is far less than for a point-source signal. The frequency band over which the amplification occurs is still smaller in the narrow swell, but the order of magnitude of the amplification is the same in the two swells. Analysing how the amplification varies with epicentral distance (Fig. 17), one notices that the gain in amplification when going from 3000 to 5000 km distance is smaller with a line-source signal than with a point-source one (Fig. 10), especially in a narrow swell. It seems that a stationary situation in terms of amplification is reached at shorter distances with a line-source than with a point-source. One also notices that at large epicentral distances, it is now in the wide swell that the amplification is the most important.

The horizontal components

The discussion up to now has been based only on the vertical component of the signals. We should also mention how the channel affects the horizontal ones. For a line-source, the displacement calculated along the x- and y-axis of the channel directly yields the longitudinal and transverse displacements. For a point-source, we rotate these displacements in the source–station direction.

The longitudinal displacements in the swell behave very

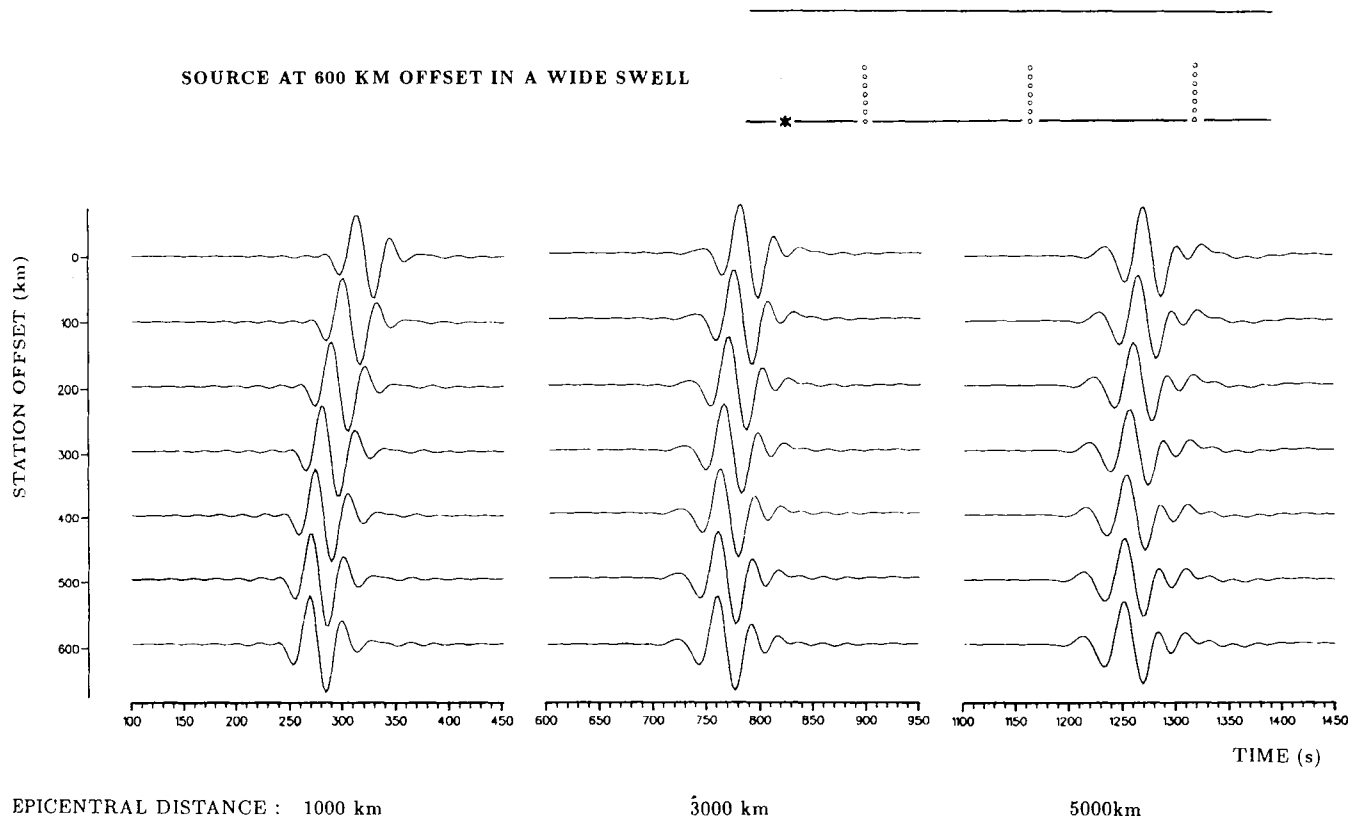

Figure 11. The same as Fig. 7 for a source offset by 600 km from the swell axis.

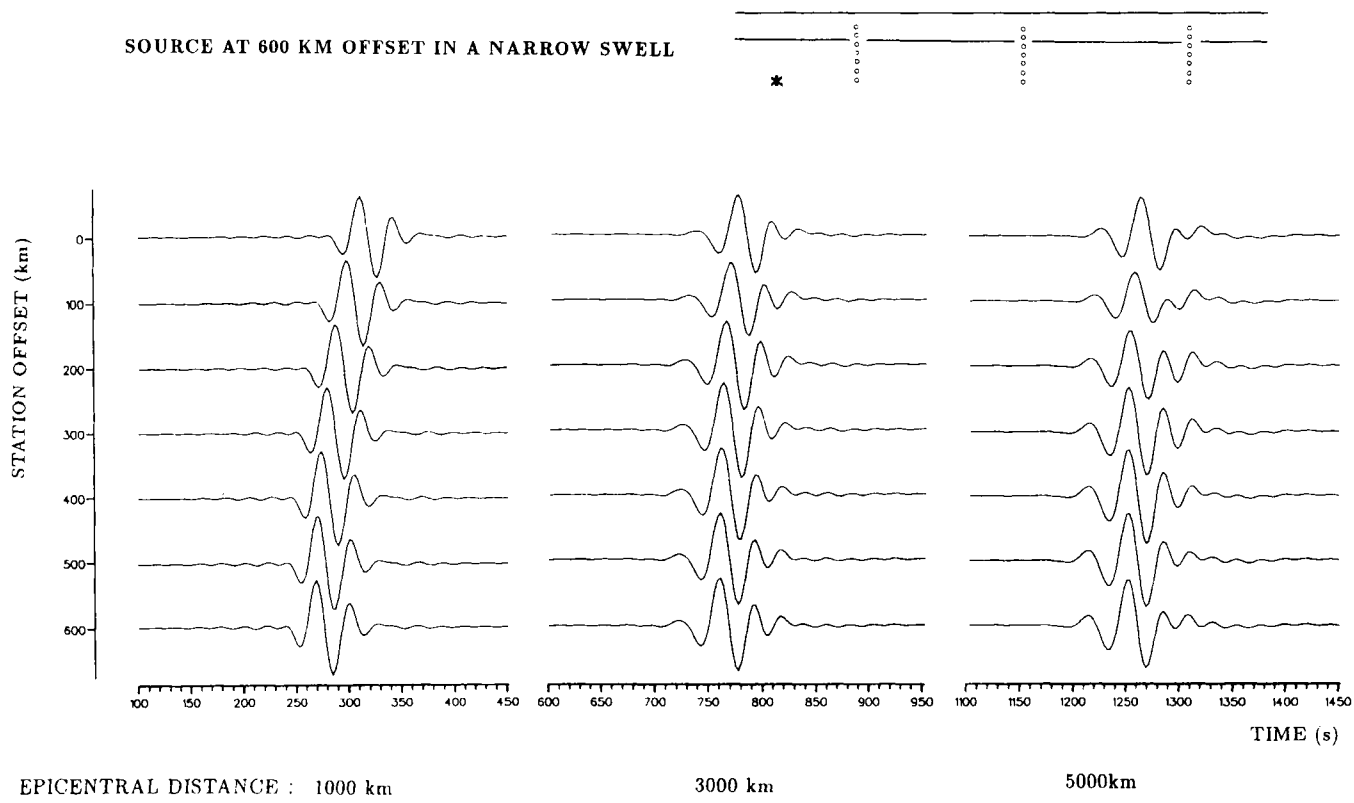

Figure 12. The same as Fig. 11 for a swell of 300 km width.

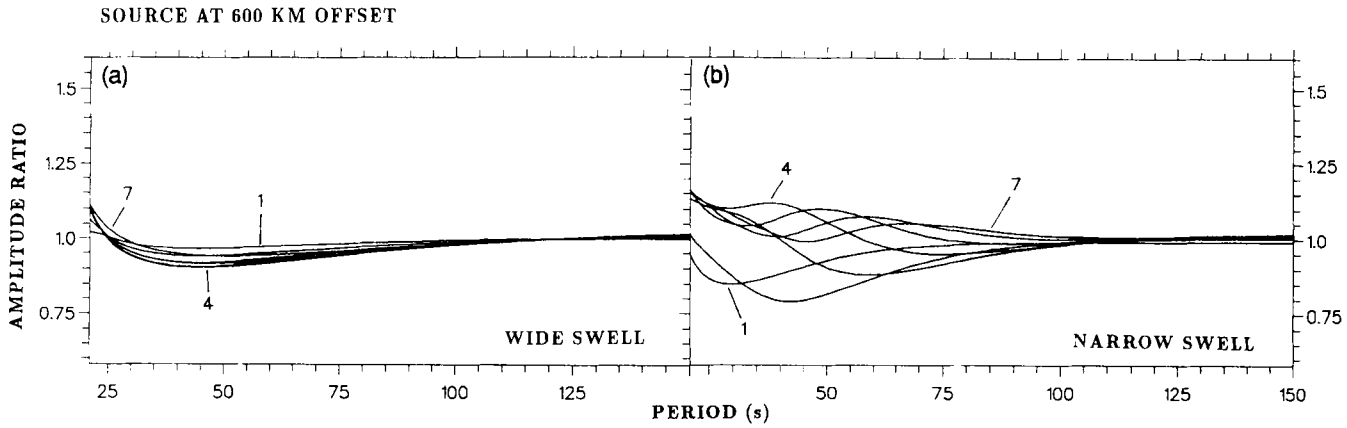

Figure 13. The same as Fig. 8 for a source offset by 600 km from the swell axes.

much like the vertical ones, both in terms of amplitude and waveform variations. They keep their quarter-of-period phase shift. Seen in the vertical plane of propagation, the wavefield has therefore the same characteristic ellipticity as in an homogeneous model.

Due to the lateral heterogeneity, some transverse components also appear in source, station and swell non-symmetric configurations. These transverse components are predominantly high frequency and are usually maximum at stations offset by 100 to 200 km from the channel axis. They reach in most cases 10 per cent of the longitudinal components at 5000 km epicentral distance, and 5 per cent at 3000 km. One exception is for a line-source in the wide swell, where an amplitude two times larger is observed. The three components of the wavefield in that case of largest computed transverse component is shown in Fig. 18. The longitudinal and transverse components are not in phase, which shows that the presence of the transverse component is a complex waveguide effect, and not only the result of a deviation of the wavepath from the great circle.

Phase velocities between two stations

Up to now, we have focused attention on the relative amplitude of the seismograms. We have not discussed the effect of the lateral heterogeneity on the wavetrain arrival

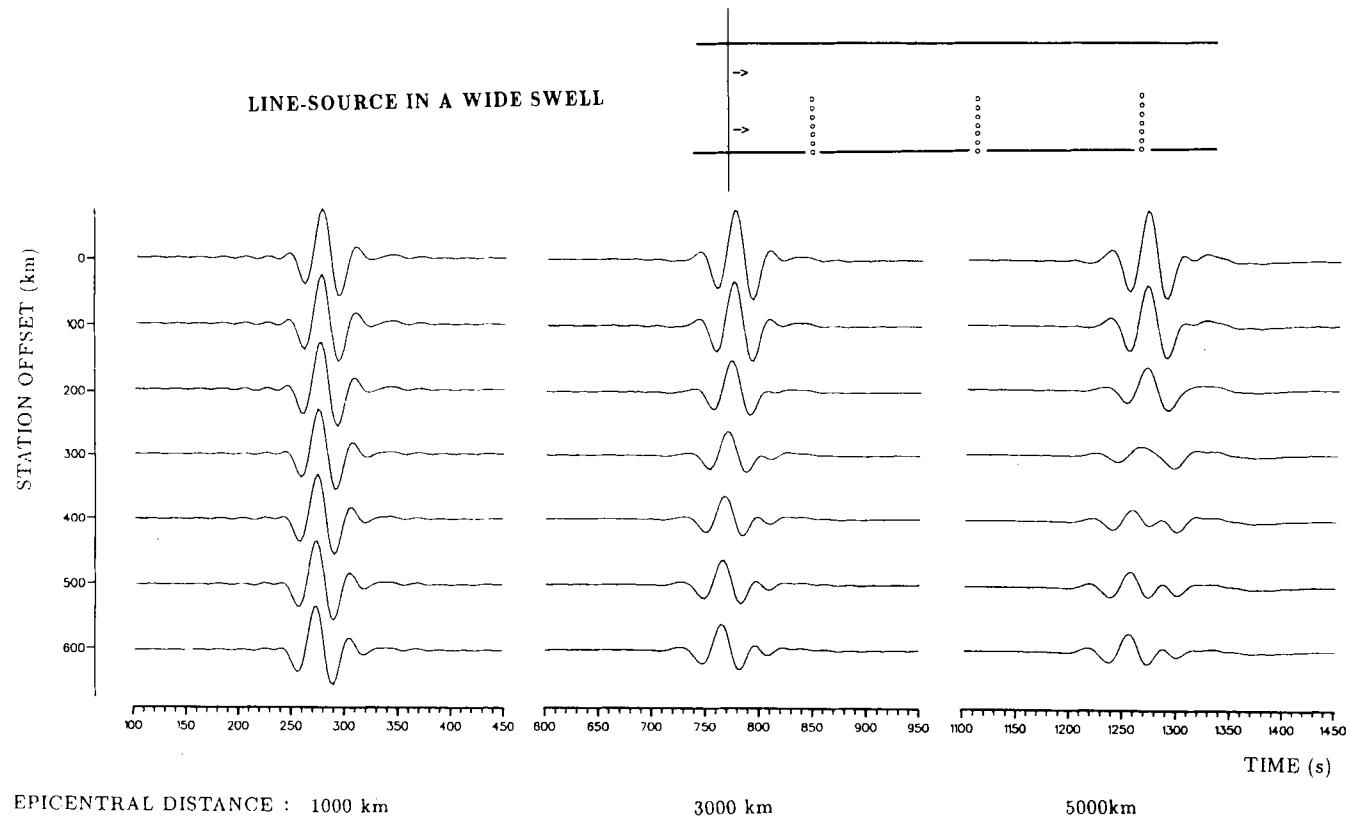

Figure 14. The same as Fig. 7 for a line-source in the 1200 km wide swell.

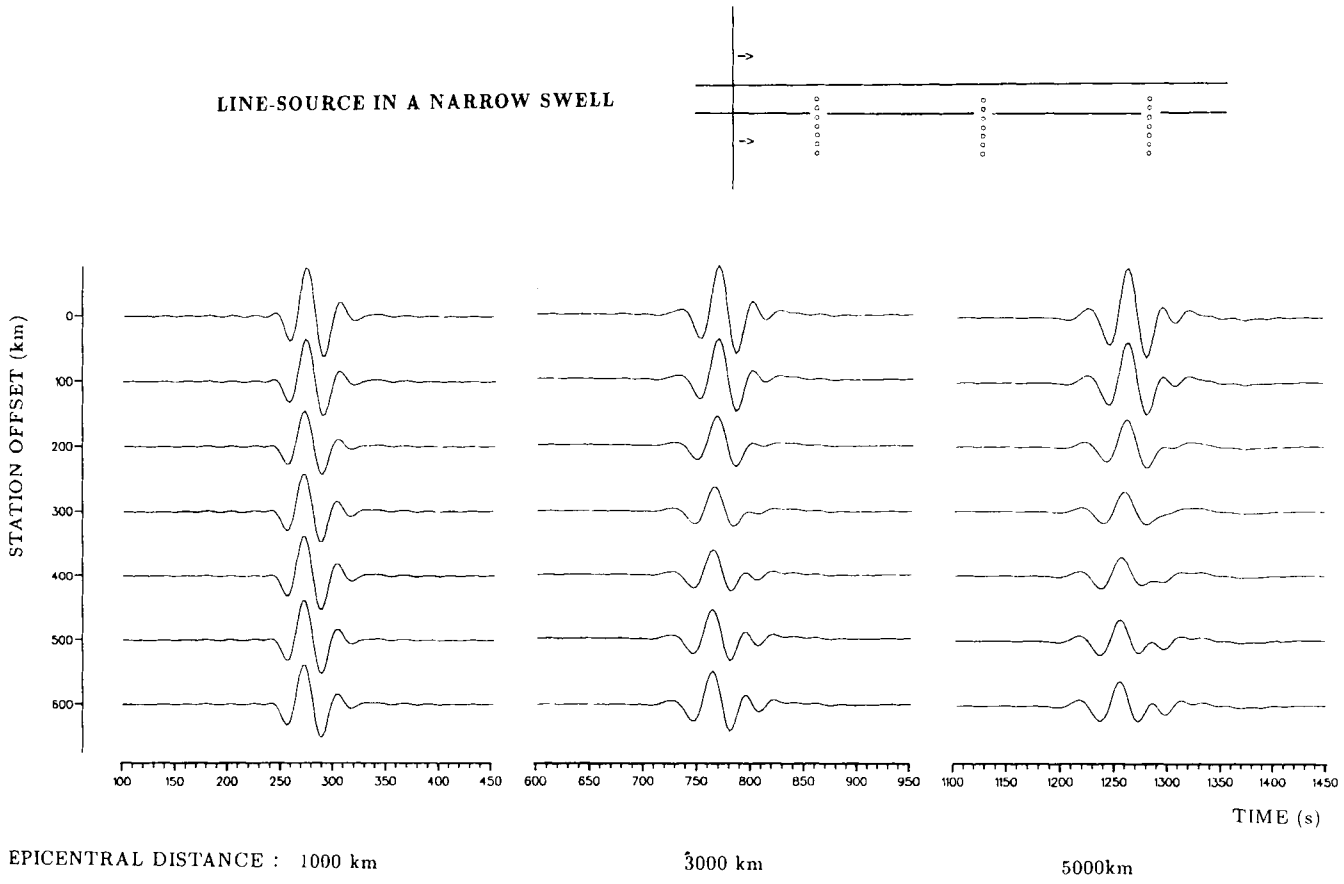

Figure 15. The same as Fig. 14 for a swell of 300 km width.

time, or more generally, on its phase and phase velocity. In order to analyse the phase characteristics of the synthetic seismograms, we calculate for the different source cases presented above, the apparent phase velocity between stations situated in the middle of the channel. The stations are situated at epicentral distances of 1000 and 3000 km, or 3000 and 5000 km. The interstation distance of 2000 km is similar to the distance between Midway and Hawaii stations. The difference between the phase spectra of the vertical components at the two stations is used directly to measure the interstation phase velocity. Only explosive source cases are presented. Phase velocities calculated with other source

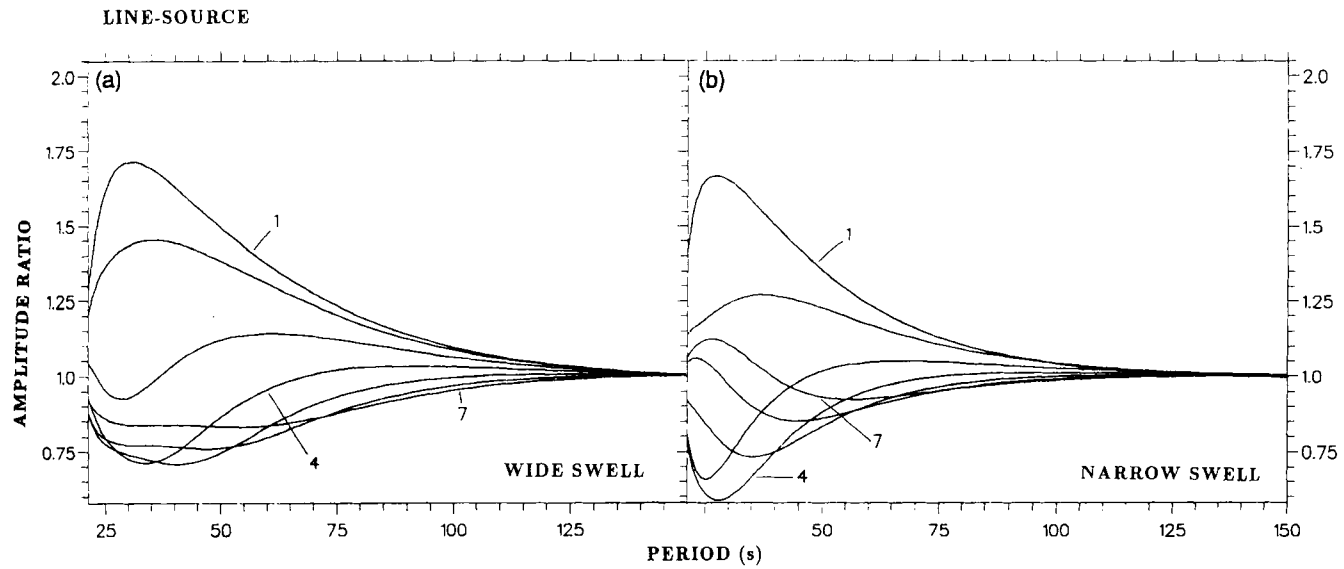

Figure 16. The same as Fig. 8 for a line-source.

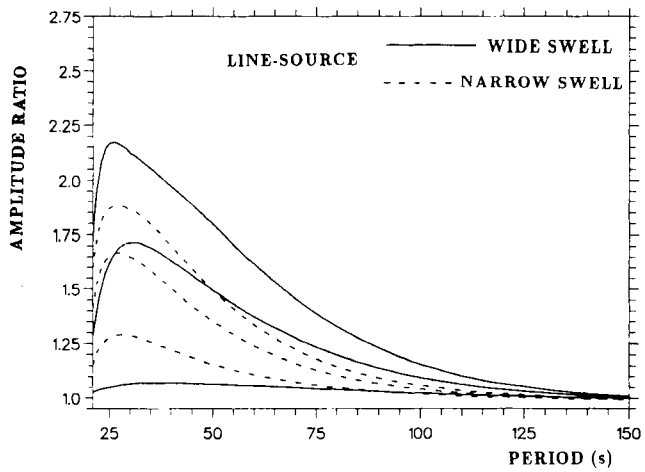

Figure 17. The same as Fig. 10 for a line-source.

mechanisms than an explosion do not show significant differences, when imposing the same restriction as for the amplification curves, namely that we are not close to a node of the radiation pattern.

In Fig. 19 are gathered six different cases of interstation apparent phase velocities. The upper bound of the period range is reduced to 120 s to enlarge the short period part of the figure, where the most interesting features are seen. On each plot, the apparent interstation phase velocities appear as short-dotted lines. The phase velocities of the Rayleigh

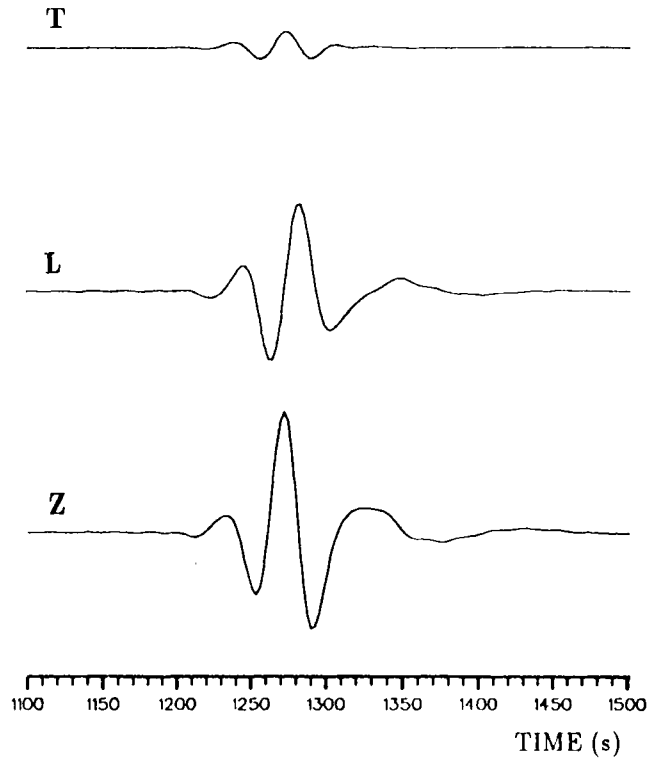

Figure 18. The three components of a Rayleigh wave synthetic seismogram for a line-source in a 1200 km wide swell. The station is at 5000 km epicentral distance and offset by 200 km from the swell axis. Timing is relative to the source time. The three components are plotted at the same scale.

wave fundamental mode in the two models of Nishimura & Forsyth (1989), which form our extreme models for the swell, and the phase velocity curves for the lateral modes of the structure are superimposed for reference.

In the wider swell, and for an explosive source situated in the middle of the channel (Fig. 19a), the interstation dispersion is little influenced by the outskirts of the structure, and the measured phase velocity is a rather good approximation of the dispersion in the middle of the swell, especially at short periods.

When the source is offset by 600 km from the channel axis, we account for the slightly smaller difference in epicentral distance between the stations. Each source–station line crosses exactly half the swell width. The mean velocity along these lines is then the average phase velocity of the structure. This agrees very well with the calculated interstation phase velocities shown in Fig. 19(c). In these cases, no effect other than the averaging of the slowness along the direct path has to be accounted for in the interpretation of the measurements.

For a line-source, the slowness average along the direct path predicts that the interstation phase velocities should be the velocity in the middle of the structure. The ones measured on the synthetic seismograms show actually a non-negligible shift towards the velocities of the outer parts of the structure (Fig. 19e). Frequency-dependent propagations off the direct wave path influence the wavefield significantly. Considering the length of the Hawaiian swell and the positions of the seismic sources and stations utilized by Lévêque (1991), it appears that the phase velocities presented for this line source and between stations at epicentral distances of 1000 and 3000 km are the most relevant ones for interepreting their data. Their data period range is 25 to 50 s. The influence of the outer part of the swell on their measured phase velocities can therefore be evaluated to be between 16 and 20 per cent.

For the more narrow swell, the dispersion curve of the unique lateral mode has a dominant influence on the interstation phase velocities, whatever the source, as illustrated in Figs 19(b), (d) and (f). A stationary situation in terms of phase velocity as a function of epicentral distance is reached much faster in the narrow swell than in the wider one. Moreover, the presence of only one lateral mode prevents the occurrence of interference phenomena which complicate the phase velocity behaviour in the wider swell at very large epicentral distances.

The effect of the Earth's sphericity

Our modelling is done assuming flat laterally heterogeneous structures. Considering the epicentral distances involved and the width of the Hawaiian swell, which amounts to 11° of the Earth's circumference, it is worth examining the possible biases introduced in our results by neglecting the Earth's sphericity.

The coupling method is derived for flat structures, but we account for the sphericity of the Earth when calculating the local modes. Considering that we are modelling waves propagating along the channel, this is equivalent to accounting for the sphericity in the channel direction, and neglecting it in the transverse direction. Our model can therefore be thought of as a cylindrical projection of the

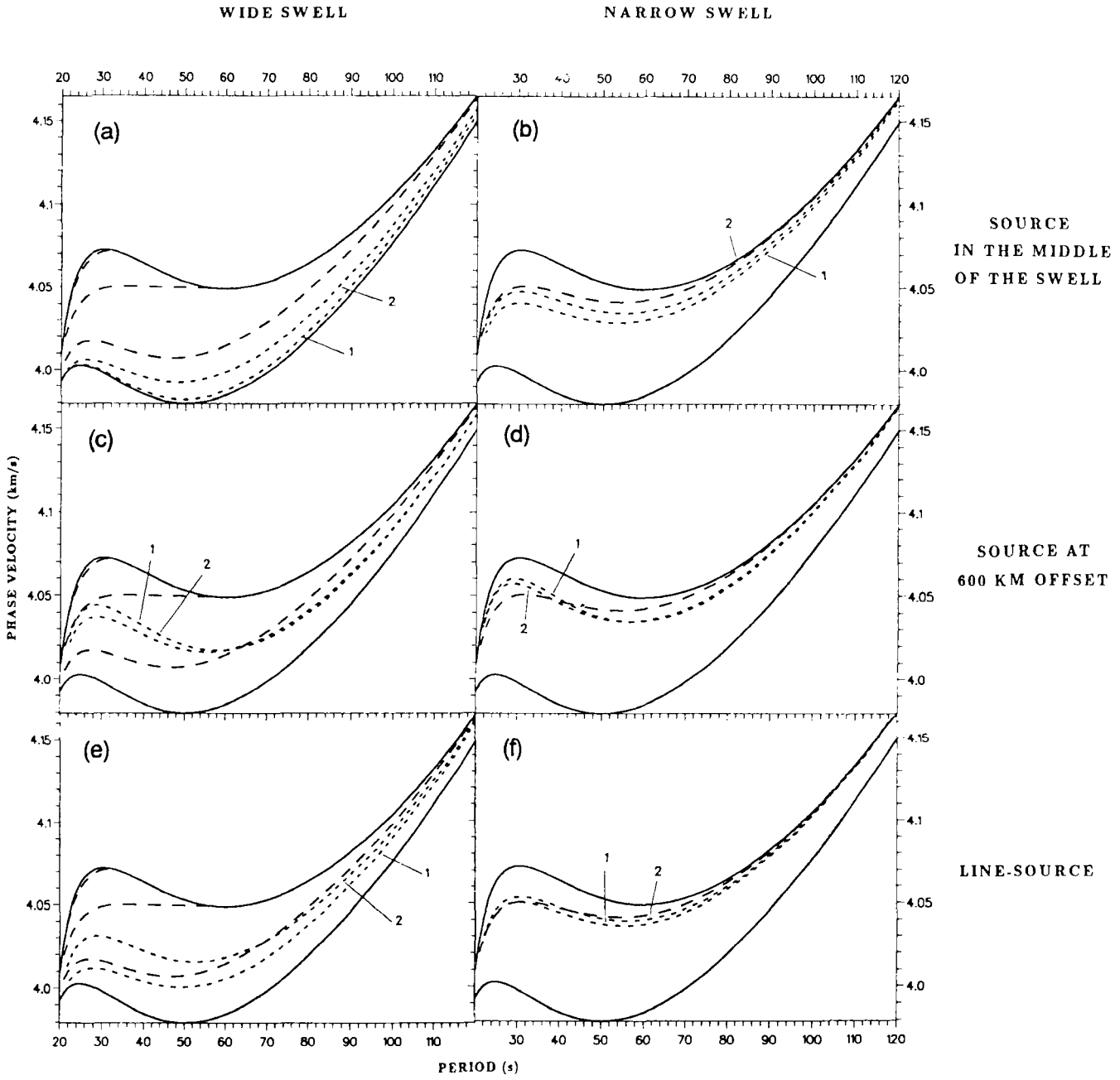

Figure 19. Interstation phase velocities measured on the vertical component of synthetic Rayleigh waves. The stations are situated in the middle of the swells at 1000 and 3000 km epicentral distance (dotted lines labelled 1) or at 3000 and 5000 km epicentral distance (dotted lines labelled 2). The phase velocities of the lateral modes (long dashed lines) and of the extreme models of the structure (solid lines) are shown for reference. Plots (a) and (b) are for an explosive source situated in the middle of the swell, plots (c) and (d) for a source 600 km offset from the swell axis, and plots (e) and (f) for a line-source. Plots (a), (c) and (e) are for a 1200 km wide swell, and plots (b), (d) and (f) for a 300 km wide swell.

Earth, as shown in Fig. 20(a). The middle of the channel on the spherical Earth is then assumed to be a great circle, chosen as reference for the cylindrical projection, and the sides of the channel are parallel small circles. The effect of the projection is to dilate the small circles to the same length as the great circle. We expect therefore that the flat structure approximation introduces a negative bias on the computed phase velocities by penalizing the waves which travel in the fastest parts of the model, away from the axis.

Jobert & Jobert (1983) have shown that it is possible to trace rays on a spherical heterogeneous Earth using algorithms developed for flat structures. Only a Mercator projection of the Earth and a simple transformation of the local velocities are needed. Their formulae applied to our problem mainly result in multiplying the local phase velocities by $1/\cos(\alpha)$, where α is the angular distance from the channel axis. This factor is actually the inverse of the dilatation introduced by the projection. Multiplying the local phase velocities in the 1200 km wide swell by this factor, we can calculate interstation phase velocities which

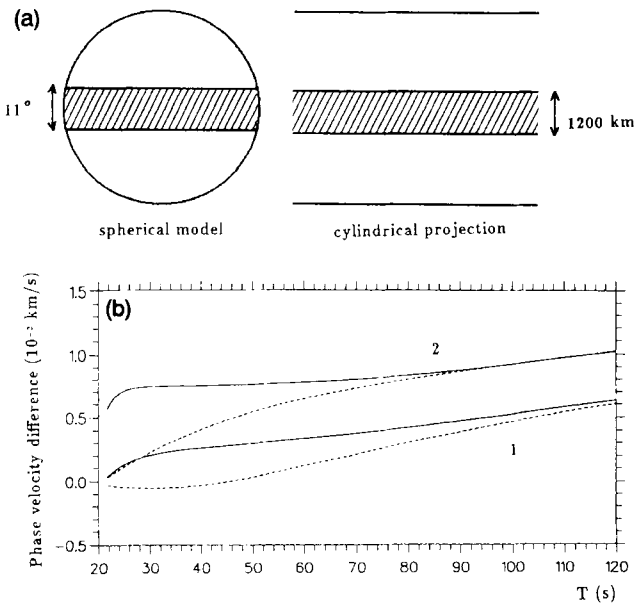

Figure 20. Plot (a)—Diagram showing a channel as a hatched zone on the spherical Earth, its cylindrical projection, and the corresponding dimensions for the Hawaiian swell. Plot (b)—Corrections brought to interstation phase velocities when correcting the local phase velocities for the Earth's sphericity using the formula of Jobert & Jobert (1983). The configuration of source and receivers is the same as on Fig. 19(e), that is a line-source and stations situated in the middle of the swell at 1000 and 3000 km (curves labelled 1) or at 3000 and 5000 km epicentral distance (curves labelled 2). The solid lines are for a 1200 km wide swell model. The dashed lines are for an homogeneous model identical to the model in middle of the swell.

account better for the Earth's sphericity. The difference between these velocities and those calculated with the ordinary flat structure are shown as solid lines in Fig. 20(b) for a line-source and the same two different configurations of receivers as in Fig. 19(e).

The velocity transformation gives an exact solution to the wave propagation problem on a spherical Earth only within the framework of ray theory. The wavelengths we are modelling are not short compared to the dimensions of the swell, and the transformation does not give an exact solution in our case. In order to test its limitations, we also apply it to a laterally homogeneous model. The deviations of the interstation phase velocities computed in that model with respect to the velocities in the fully homogeneous model can be considered as the bias introduced by the inadequacy of the transformation at long wavelengths. They are plotted as dashed lines in Fig. 20(b). The actual correction to be applied to the phase velocities in Fig. 19(e) in order to account for the sphericity of the Earth is the difference between the solid and dashed curves in Fig. 20(b), i.e. the velocity perturbation introduced by transforming the model minus the bias introduced by the transformation itself. It is very small at long periods. The maximum correction is $0.005\,km\,s^{-1}$ at 20 s of period. It is $0.003\,km\,s^{-1}$ for the period range and epicentral distances most suitable to interpret the data of Lévêque (1991), i.e. 3 per cent of the total velocity variation in the swell. It is small but not negligible compared to the effect of the swell itself in the flat approximation, which we recall to be between 16 and 26 per cent. For a point-source along the swell axis, the maximum correction is $0.0025\,km\,s^{-1}$ at 60 s of period for stations at 3000 km and 5000 km epicentral distance.

Using the same procedure, we analyse the effect of sphericity on the signal amplification due to the swell. We find no significant difference relative to the amplification calculated in flat structures for epicentral distances up to 3000 km. The amplification decreases by 15 per cent for a line source, and increases by 5 per cent for a point source at 5000 km epicentral distance. These differences can be considered as negligible compared to the precision with which surface wave amplitudes can usually be modelled.

Finally, we can note that in our period range the correction introduced by the velocity transformation is comparable in magnitude to the bias due to its inadequacy at long wavelengths. Using the transformed model rather than the ordinary flat one is therefore appropriate only when these two effects can be subtracted from each other, and would not provide for example more accurate waveforms.

CONCLUSION

We have synthetized seismograms in a realistic model of the Hawaiian swell, in order to refine the interpretation of Rayleigh wave phase velocities measured by Lévêque (1991) in between Midway and Hawaii broad-band stations. The influence on the interstation phase velocities of the outer parts of this elongated 2-D structure, along which the waves propagate, has been quantified. We find that for a realistic swell width of 1200 km, the influence of the faster lithosphere outside the swell on the phase velocities measured in the centre of the structure is of the order of 20 to 30 per cent. This influence is not negligible, but is still small enough for the seismological data to be able to bring new information about the lithospheric structure under the Hawaiian chain, and to indicate if they corroborate the reheating model for the swell, based on geoid and heat-flow data.

The modellings also demonstrate how the channel acts as a waveguide which amplifies and modifies the signal. The amplification, analysed in the frequency domain, is varying with source position and epicentral distance. It is maximum for sources situated on the axis of the channel and for line-sources across at right angles. It usually reaches values of 1.5 to 2.0 in these situations.

In order to calculate the synthetic seismograms in the Hawaiian swell, the local mode coupling method of Maupin (1988) has been extended. We now have a very complete tool which can be used to calculate surface waves synthetic seismograms for any source–station configuration in smooth, anelastic 2-D structure. It accounts for mode coupling effects, including Rayleigh–Love coupling. It also reveals the characteristics of the lateral modes of the 2-D structure.

REFERENCES

Bostock, M. G., 1991. Surface-wave scattering from 3-D obstacles, *Geophys. J. Int.*, **104**, 351–370.

Detrick, R. S. & Crough, S. T., 1978. Island subsidence, hot-spots, and lithospheric thinning, *J. geophys. Res.*, **83,** 1236–1244.

Forsyth, D. W., 1977. The evolution of the upper mantle beneath mid-ocean ridges, *Tectonophysics,* **38,** 89–118.

Fraser, L. N. & Gettrust, J. F., 1984. On a generalization of Filon's method and the computation of the oscillatory integrals of seismology, *Geophys. J. R. astr. Soc.*, **76,** 461–481.

Gregersen, S., 1978. Possible mode conversion between Love and Rayleigh waves at a continental margin, *Geophys. J. R. astr. Soc.*, **54,** 121–127.

Jobert, N. & Jobert, G., 1983. An application of ray theory to the propagation of waves along a laterally heterogeneous spherical structure, *Geophys. Res. Lett.*, **10,** 1148–1151.

Kennett, B. L. N., 1984. Guided-wave propagation in laterally varying media. I. Theoretical development, *Geophys. J. R. astr. Soc.*, **79,** 235–255.

Lévêque, J.-J., 1991. *Inversion of phase velocity data related to the Hawaiian swell: effect of anisotropy (abstract)*, p. 87, IASPEI meeting, Vienna.

Lognonné, Ph., 1991. Normal modes and seismograms in an anelastic rotating Earth, *J. geophys. Res.*, **96,** 20 309–20 319.

Love, A. E. H., 1927. *A Treatise on the Mathematical Theory of Elasticity,* Cambridge University Press, London.

Maupin, V., 1988. Surface waves across 2-D structures: a method based on coupled local modes, *Geophys. J.*, **93,** 173–185.

Maupin, V. & Kennett, B. L. N., 1987. On the use of truncated modal extensions in laterally varying media, *Geophys. J. R. astr. Soc.*, **91,** 837–851.

Montagner, J.-P. & Jobert, N., 1981. Investigation of upper mantle structure under young regions of the southeast Pacific using long-period Rayleigh waves, *Phys. Earth planet. Inter.*, **27,** 206–222.

Nishimura, C. & Forsyth, D. W., 1989. The anisotropic structure of the upper mantle in the Pacific, *Geophys. J.*, **96,** 203–226.

Saito, M., 1988. Disper80: a subroutine package for the calculation of seismic normal mode solutions, in *Seismological Algorithms,* pp. 293–319, ed. Doornbos, D. J., Academic Press, New York.

Snieder, R., 1986. 3-D linearized scattering of surface waves and a formalism for surface wave holography, *Geophys. J. R. astr. Soc.*, **84,** 581–605.

Takeuchi, H. & Saito, M., 1972. Seismic surface waves, in *Methods in Computational Physics,* vol. 11, pp. 217–295, Academic Press, New York.

Woods, M. T., Lévêque, J.-J., Okal, E. A. & Cara, M., 1991. Two-station measurements of Rayleigh wave group velocity along the Hawai'ian swell, *Geophys. Res. Lett.*, **18,** 105–108.

APPENDIX A: ORTHOGONALITY AND SYMMETRY RELATIONS

Symmetry relations between primal and dual modes

In order to express these symmetry relations, we first need to detail the structure of the operator **A** in transverse isotropic models. The operator elements are given for isotropic models in M88, appendix 3. In transverse isotropic models, using the six elastic coefficients defined by Love (1927), they are:

$$\mathbf{C}_{11}^{-1} = \begin{pmatrix} 1/A & 0 & 0 \\ 0 & 1/N & 0 \\ 0 & 0 & 1/L \end{pmatrix};$$

$$\mathbf{C}_{11}^{-1}\mathbf{C}_{12} = \begin{pmatrix} 0 & (A-2N)/A & 0 \\ 1 & 0 & 0 \\ 0 & 0 & 0 \end{pmatrix};$$

$$\mathbf{C}_{11}^{-1}\mathbf{C}_{13} = \begin{pmatrix} 0 & 0 & F/A \\ 0 & 0 & 0 \\ 1 & 0 & 0 \end{pmatrix};\quad \mathbf{Q}_{22} = \begin{pmatrix} 0 & 0 & 0 \\ 0 & 4N(A-N)/A & 0 \\ 0 & 0 & L \end{pmatrix}$$

$$\mathbf{Q}_{23} = \begin{pmatrix} 0 & 0 & 0 \\ 0 & 0 & 2NF/A \\ 0 & L & 0 \end{pmatrix};\quad \mathbf{Q}_{33} = \begin{pmatrix} 0 & 0 & 0 \\ 0 & L & 0 \\ 0 & 0 & (AC-F^2)/A \end{pmatrix}$$

We recall the form of the operator **A**:

$$\mathbf{A} = \begin{pmatrix} & & -\mathbf{C}_{11}^{-1}\mathbf{C}_{13}\dfrac{\partial}{\partial z} + \mathbf{C}_{11}^{-1}\mathbf{C}_{12}ip \\ -\rho\omega^2 - \dfrac{\partial}{\partial x}\mathbf{Q}_{33}\dfrac{\partial}{\partial z} + ip\mathbf{Q}_{23}\dfrac{\partial}{\partial z} + \dfrac{\partial}{\partial z}(\mathbf{Q}_{33}ip) + p^2\mathbf{Q}_{22} & & \\ & & \mathbf{C}_{11}^{-1} \\ & & -\dfrac{\partial}{\partial z}\mathbf{C}_{31}\mathbf{C}_{11}^{-1} + ip\mathbf{C}_{21}\mathbf{C}_{11}^{-1} \end{pmatrix}$$

In order to construct the dual operator $\mathbf{A}^{\#}$, we change p into $-p$ in **A**. This is equivalent to multiplying the different elements in **A** by some ± 1 factors:

$$\begin{pmatrix} 0 & -1 & +1 & +1 & 0 & 0 \\ -1 & 0 & 0 & 0 & +1 & 0 \\ +1 & 0 & 0 & 0 & 0 & +1 \\ +1 & 0 & 0 & 0 & -1 & +1 \\ 0 & +1 & -1 & -1 & 0 & 0 \\ 0 & -1 & +1 & +1 & 0 & 0 \end{pmatrix}$$

The dual mode satisfy the same equation as the primal mode changing **A** into $\mathbf{A}^{\#}$ and $-k_i$ into k_i. The eigenfunctions of a dual mode can therefore be found by multiplying the elements of the primal mode eigenfunction by:

$$\begin{pmatrix} +1 \\ +1 \\ -1 \\ -1 \\ -1 \\ +1 \end{pmatrix}$$

Symmetry properties and bi-orthogonality

Instead of writing in details the proof of the primal and dual modes bi-orthogonality, we indicate how to derive it from the proof given for the former scalar product in appendix 2 of M88 (A2).

The new scalar product no longer involves complex conjugation of the first mode in the product, but the use of its dual mode. Moreover, the i factor has disappeared. Therefore, the first two equations in A2 can be rewritten for the new scalar product omitting the i factor in front of the integral sign, and changing the complex conjugation signs * by the dual mode signs #. The third equation can also be rewritten with exactly the same modifications. The terms with factors ip had changed sign in A2 due to the complex conjugation in the scalar product, whereas they now change because we are using the dual operator. The result is of course the same and we can write:

$$\langle \mathbf{u}_q^{\#}, \mathbf{A}\mathbf{u}_r \rangle - \sum_n [w_q^{\#} t_{3r}] = -\langle \mathbf{A}^{\#}\mathbf{u}_q^{\#}, \mathbf{u}_r \rangle - \sum_n [t_{3q}^{\#} w_r]. \quad \text{(A1)}$$

For modes which satisfy flat boundary continuity conditions and the equations of motion (3) and (5), this can be written:

$$i(k_q - k_r)\langle \mathbf{u}_q^{\#}, \mathbf{u}_r \rangle = 0.$$

If $\mathbf{u}_q^{\#}$ and $\mathbf{u}_r$ are not dual modes of each other, their wavenumbers are different, except in some peculiar cases of mode degeneracy. Therefore, we obtain the bi-orthogonality relation:

$$\langle \mathbf{u}_q^{\#}, \mathbf{u}_r \rangle = 0 \quad \text{for } r \neq q.$$

Since it does not involve complex conjugation, this bi-orthogonality relation is also valid for anelastic models with complex elastic coefficients.

The symmetrized scalar product

We define the symmetrized scalar product:

$$\left\langle \mathbf{u}_q^{\#}, \frac{\partial \mathbf{A}}{\partial x}, \mathbf{u}_r \right\rangle = \left\langle \mathbf{A}^{\#}\mathbf{u}_q^{\#}, \frac{\partial \mathbf{u}_r}{\partial x} \right\rangle + \left\langle \mathbf{u}_q^{\#}, \mathbf{A}\frac{\partial \mathbf{u}_r}{\partial x} \right\rangle + \left\langle \mathbf{u}_q^{\#}, \frac{\partial \mathbf{A}}{\partial x}\mathbf{u}_r \right\rangle.$$

Using the symmetry relation (A1) and the same procedure as in M88, equations (19)–(24), we can show that $\left\langle \mathbf{u}_q^{\#}, \frac{\partial \mathbf{A}}{\partial x}, \mathbf{u}_r \right\rangle$ equals the right-hand side of equation (24) in M88, replacing the complex conjugation signs * by the dual mode signs #.

APPENDIX B: RAYLEIGH AND LOVE BASIC MODES

Definition of forward and backward modes

The basic modes are defined as combination of forward and backward modes (equation 9). For modes with real wavenumbers, the concept of forward and backward mode is clear: modes with real positive wavenumber k_i propagate forwards in x, and modes with real negative wavenumbers propagate backwards in x. We need to define it more precisely for the modes with complex wavenumbers.

In boundary conditions, the condition of only forward propagating modes on one side of the model is associated with the condition that only exponentially decreasing waves are present on this same side. Therefore, we define as forward modes those with $\mathcal{I}m\ (k) < 0$, or $\mathcal{I}m\ (k) = 0$ and $\mathcal{R}e\ (k) > 0$. The backward modes are defined as the modes having wavenumbers in the complementary part of the complex k-plane.

Rayleigh and Love basic modes

The primal basic modes for Rayleigh waves in transverse isotropic models are:

$$\mathbf{u}^{+} = \begin{pmatrix} 0 \\ pu/K \\ w \\ A(-iKu) + F\dfrac{\partial w}{\partial z} + 2iN\dfrac{p^2}{K}u \\ 0 \\ 0 \end{pmatrix},$$

$$\mathbf{u}^{-} = \begin{pmatrix} iu/K \\ 0 \\ 0 \\ 0 \\ 2Npu/K \\ L\left(\dfrac{i}{K}\dfrac{\partial u}{\partial z} + w\right) \end{pmatrix},$$

where w is the vertical and u is the longitudinal classic displacement of the Rayleigh wave mode.

The primal basic modes for Love waves are:

$$\mathbf{u}^{+} = \begin{pmatrix} -pv/K \\ 0 \\ 0 \\ 0 \\ -iN\dfrac{k^2 - p^2}{K}v \\ -L\dfrac{p}{K}\dfrac{\partial v}{\partial z} \end{pmatrix}, \qquad \mathbf{u}^{-} = \begin{pmatrix} 0 \\ iv/K \\ 0 \\ -2N\dfrac{p}{K}v \\ 0 \\ 0 \end{pmatrix}$$

where v is the classic transversal displacement of the Love-wave mode.